# Magnetic Circular Dichroism Spectroscopic Studies of Mononuclear Non-Heme Ferrous Model Complexes. Correlation of Excited- and Ground-State Electronic Structure with Geometry

**Elizabeth G. Pavel,[†] Nobumasa Kitajima,[‡] and Edward I. Solomon*[,†]**

*Contribution from the Department of Chemistry, Stanford University, Stanford, California 94305, and Research Laboratory of Resources Utilization, Tokyo Institute of Technology, 4259 Nagatsuta, Midori-ku, Yokohama, 226 Japan*

*Received October 28, 1997*

**Abstract:** Mononuclear non-heme iron enzymes catalyze a variety of biologically important reactions involving dioxygen, and yet, the non-heme ferrous active sites have been difficult to study by most spectroscopic methods. A combination of near-infrared (NIR) magnetic circular dichroism (MCD) and variable-temperature, variable-field (VTVH) MCD spectroscopies has been applied to 24 structurally defined mononuclear non-heme ferrous model complexes to rigorously correlate spectral data with geometric and electronic structure. While general trends for the excited-state splittings have been predicted by ligand field theory, these predictions are now evaluated by systematically studying the NIR MCD spectra of a series of high-spin ($S = 2$) ferrous models with a wide range of coordination numbers and geometries. VTVH MCD spectroscopy is used to probe ground-state electronic structure, and a complete MCD intensity expression for non-Kramers systems that includes *z*-polarization, *B*-terms, and excited states has been derived. This expression has been applied to these model complexes to determine signs of the zero-field splitting and to obtain ground-state spin-Hamiltonian parameters, which can be related to ground-state ligand field splittings. These experimental ground-state data are used to develop the information content available from VTVH MCD, in particular the ability to probe specific metal−ligand bonding interactions for different coordination environments. The excited-state ligand field data are used to construct a set of spectroscopic guidelines which, combined with the ground-state information, allow one to clearly determine the coordination number and geometry of an unknown ferrous center, with the exception of only a few ambiguous cases. Additionally, the MCD data provide insight into the origin of the MCD *C*-term intensities and signs for low-symmetry ferrous centers. The results obtained through these model studies now provide the basis for investigating ferrous active sites of non-heme iron enzymes to probe the geometric and electronic structure of a site with respect to oxygen reactivity and understanding how differences in structure correlate with differences in reactivity.

## Introduction

Non-heme iron active sites are present in a wide range of enzymes performing a variety of important biological functions involving dioxygen.[1,2] Unlike heme or iron−sulfur systems, non-heme iron centers are considerably less spectroscopically accessible, particularly the ferrous sites, which lack intense low-energy charge-transfer transitions and are often silent in electron paramagnetic resonance (EPR). A spectroscopic protocol has therefore been developed to probe high-spin ($S = 2$) non-heme ferrous sites utilizing near-infrared (NIR) magnetic circular dichroism (MCD) spectroscopy to observe excited-state ligand field splittings and variable-temperature, variable-field (VTVH) MCD to obtain the ground-state sublevel splittings.[3−5] The $^5D$ ground state for high-spin $Fe^{2+}$ ($d^6$) is split under octahedral symmetry into a $^5T_{2g}$ ground state and a $^5E_g$ excited state, separated by $10Dq \approx 10\,000$ cm$^{-1}$ for biologically relevant N and O ligands. Because the $^5T_{2g} \rightarrow {}^5E_g$ transition corresponds to the $(t_{2g})^4(e_g)^2 \rightarrow (t_{2g})^3(e_g)^3$ one-electron promotion, the splitting of the $^5E_g$ excited state reflects the separation of the $e_g$ orbitals which is sensitive to the geometry of the site. For less than octahedral symmetry, the double degeneracy of the excited state is removed, and this splitting, $\Delta^5E_g \equiv E(d_{x^2-y^2}) - E(d_{z^2})$, is sensitive to coordination number and geometry. NIR MCD spectroscopy permits the direct observation of these ligand field excited states which are difficult to see in absorption spectroscopy, particularly for metalloproteins due to low extinction coefficients and overlap with protein and buffer vibrations in the NIR spectral region. Ligand field calculations and studies on a limited number of model complexes have predicted general trends for the NIR transition energies as related to the geometric environment about a ferrous center.[3,5,6]

VTVH MCD is used to obtain ground-state electronic structure information and sublevel splittings. The $S = 2$ spin manifold for high-spin $Fe^{2+}$ undergoes axial zero-field splitting (ZFS) into $M_S = 0$, $\pm1$, and $\pm2$ components separated by $D$ and $3D$, respectively. For negative ZFS ($D < 0$), the non-

[†] Stanford University.
[‡] Tokyo Institute of Technology.

(1) Feig, A. L.; Lippard, S. J. *Chem. Rev.* **1994**, *94*, 759−805.
(2) Que, L., Jr.; Ho, R. Y. N. *Chem. Rev.* **1996**, *96*, 2607−2624.
(3) Solomon, E. I.; Pavel, E. G.; Loeb, K. E.; Campochiaro, C. *Coord. Chem. Rev.* **1995**, *144*, 369−460.
(4) Solomon, E. I.; Zhang, Y. *Acc. Chem. Res.* **1992**, *25*, 343−352.
(5) Whittaker, J. W.; Solomon, E. I. *J. Am. Chem. Soc.* **1988**, *110*, 5329−5339.
(6) Pulver, S.; Froland, W. A.; Fox, B. G.; Lipscomb, J. D.; Solomon, E. I. *J. Am. Chem. Soc.* **1993**, *115*, 12409−12422.

S0002-7863(97)03735-9 CCC: $15.00 
Published on Web 04/04/1998

Kramers $M_S = \pm 2$ doublet is lowest in energy and is further split under a rhombic distortion by an amount $\delta$. The VTVH MCD data of the $M_S = \pm 2$ ground state display unusual nesting behavior, which can be explained in terms of this rhombic ZFS and a nonlinear magnetic field dependence of the wave functions.[5] For positive ZFS ($D > 0$), the $M_S = 0$ singlet is lowest in energy with the $M_S = \pm 1$ doublet at $D$ cm$^{-1}$ above. It has been shown that these systems can display VTVH MCD behavior qualitatively similar to that observed for −ZFS, but with larger nesting due to the fact that the associated zero-field splitting is governed by $D\,(2(D^2 + 3E^2)^{1/2} - D - 3E$ if rhombic ZFS is included) rather than $\delta$, where $D$ is much larger than $\delta$.[7] For both positive and negative ZFS systems, the VTVH MCD data are analyzed to extract the ground-state spin-Hamiltonian parameters ($\delta$ and $g_{\|}$ for −ZFS and $D$ and $E$ for +ZFS), which can in turn be related to the axial ($\Delta \equiv E(d_{xz,yz}) - E(d_{xy})$) and rhombic ($V \equiv E(d_{xz}) - E(d_{yz})$) ligand field splittings of the $^5T_{2g}$ ground state.[3] Because the $t_{2g}$ orbitals are sensitive to $\pi$-bonding effects, these $^5T_{2g}$ splittings probe metal−ligand $\pi$-interactions and thus can complement the excited-state data.

This methodology has been applied to a number of mononuclear non-heme ferrous enzymes to understand catalytic mechanism on a molecular level and to probe structure/function correlations as they relate to reactivity: superoxide dismutase,[5] catechol 2,3-dioxygenase,[8] phthalate dioxygenase,[9] bleomycin,[10] lipoxygenases,[11] phenylalanine hydroxylase,[12] and clavaminate synthase.[13] Application to small inorganic complexes, however, has been limited to a few structurally defined models.[5,7] In this study, we now investigate a broad series of mononuclear high-spin ferrous model complexes with varying coordination numbers and a range of geometries to correlate observed spectral features and electronic structure with geometric structure. MCD data have been collected for 24 model complexes which are structurally defined in either their ferrous or isostructural forms.[14−36] These are shown in Figure 1 and listed in Table 1 along with the ligand types and approximate site geometry.[37] The model complexes were chosen so as to cover six- (6C), five- (5C), and four-coordinate (4C) environments and a variety of geometric distortions with predominantly biologically relevant O and N ligands. The 6C models range from ferrous hexaaquo and hexaimidazole complexes to models with mixed N and O ligation. The 6C ferrous site in $FeCl_2$ has been included to probe the effects of different ligand field strengths at a distorted octahedral ferrous center (Cl vs N/O). The 5C models are divided into those with approximate square pyramidal geometry and those with approximate trigonal bipyramidal geometry. Some of these are distorted from the ideal parent geometry as would be found in low-symmetry protein environments. The 4C models include near-tetrahedral complexes with Cl ligands and a series of trigonally distorted complexes that have three N ligands and a varied unique fourth ligand (Cl, O, or S).

NIR MCD spectra have been measured and Gaussian fit for each model complex to determine the ligand field transition energies, and these are used to experimentally evaluate the trends in excited-state energies predicted by ligand field theory. The data are also used to determine experimentally the *C*-term signs and intensities for ferrous centers with different coordination numbers and geometric environments. A new closed-form MCD intensity expression including both *xy*- and *z*-polarized *C*-term contributions, along with those of temperature-independent *B*-terms and excited states, has been developed for analyzing saturation magnetization behavior. This expression is applied to the VTVH MCD data collected for 19 ferrous models to determine signs of the ZFS and to extract ground-state spin-Hamiltonian parameters. These data are used to obtain ligand field splittings and descriptions of the ground state, which combined with the observed excited-state transitions give a complete description of the d-orbitals of the ferrous center. The results are evaluated to obtain a set of guidelines for determining the structure of a given ferrous site and to develop the information content available from the ground state with respect to electronic structure and specific metal−ligand bonding interactions. Additionally, insight is obtained into the origin of the observed MCD *C*-term intensities and signs for low-symmetry ferrous sites. This correlation of spectral data with detailed geometric and electronic information provides a basis

(7) Campochiaro, C.; Pavel, E. G.; Solomon, E. I. *Inorg. Chem.* **1995**, *34*, 4669−4675.
(8) Mabrouk, P. A.; Orville, A. M.; Lipscomb, J. D.; Solomon, E. I. *J. Am. Chem. Soc.* **1991**, *113*, 4053−4061.
(9) Pavel, E. G.; Martins, L. J.; Ellis, W. R., Jr.; Solomon, E. I. *Chem. Biol.* **1994**, *1*, 173−183.
(10) Loeb, K. E.; Zaleski, J. M.; Westre, T. E.; Guajardo, R. J.; Mascharak, P. K.; Hedman, B.; Hodgson, K. O.; Solomon, E. I. *J. Am. Chem. Soc.* **1995**, *117*, 4545−4561.
(11) Pavlosky, M. A.; Zhang, Y.; Westre, T. E.; Gan, Q.-F.; Pavel, E. G.; Campochiaro, C.; Hedman, B.; Hodgson, K. O.; Solomon, E. I. *J. Am. Chem. Soc.* **1995**, *117*, 4316−4327.
(12) Loeb, K. E.; Westre, T. E.; Kappock, T. J.; Mitić, N.; Glasfeld, E.; Caradonna, J. P.; Hedman, B.; Hodgson, K. O.; Solomon, E. I. *J. Am. Chem. Soc.* **1997**, *119*, 1901−1915.
(13) Pavel, E. G.; Zhou, J.; Busby, R. W.; Gunsior, M.; Townsend, C. A.; Solomon, E. I. *J. Am. Chem. Soc.* **1998**, *120*, 743−753.
(14) Price, D. C. *Can. J. Phys.* **1987**, *65*, 1280−1293.
(15) Hamilton, W. C. *Acta Crystallogr.* **1962**, *15*, 353−360.
(16) Montgomery, H.; Chastain, R. V.; Natt, J. J.; Witkowska, A. M.; Lingafelter, E. C. *Acta Crystallogr.* **1967**, *22*, 775−780.
(17) Burbridge, C. D.; Goodgame, D. M. L. *Inorg. Chim. Acta* **1970**, *4*, 231−234.
(18) Miller, L. L.; Jacobson, R. A.; Chen, Y.-S.; Kurtz, D. M., Jr. *Acta Crystallogr.* **1989**, *C45*, 527−529.
(19) Jonas, R. T.; Stack, T. D. P. *J. Am. Chem. Soc.* **1997**, *119*, 8566−8567.
(20) Guajardo, R. J.; Hudson, S. E.; Brown, S. J.; Mascharak, P. K. *J. Am. Chem. Soc.* **1993**, *115*, 7971−7977.
(21) Tan, J. D.; Hudson, S. E.; Brown, S. J.; Olmstead, M. M.; Mascharak, P. K. *J. Am. Chem. Soc.* **1992**, *114*, 3841−3853.
(22) Crystallographic information is pending growth of crystals that are suitable for X-ray diffraction (Caradonna, J. P., personal communication).
(23) Ferrari, A.; Braibanti, A.; Bigliardi, G. *Acta Crystallogr.* **1963**, *16*, 846−847.
(24) Kitajima, N.; Tamura, N.; Amagai, H.; Fukui, H.; Moro-oka, Y.; Mizutani, Y.; Kitagawa, T.; Mathur, R.; Heerwegh, K.; Reed, C. A.; Randall, C. R.; Que, L., Jr.; Tatsumi, K. *J. Am. Chem. Soc.* **1994**, *116*, 9071−9085.
(25) Kitajima, N.; Amagai, H.; Tamura, N.; Ito, M.; Moro-oka, Y.; Heerwegh, K.; Pénicaud, A.; Mathur, R.; Reed, C. A.; Boyd, P. D. W. *Inorg. Chem.* **1993**, *32*, 3583−3584.
(26) Hodges, K. D.; Wollmann, R. G.; Barefield, E. K.; Hendrickson, D. N. *Inorg. Chem.* **1977**, *16*, 2746−2751.
(27) Hodges, K. D.; Wollmann, R. G.; Kessel, S. L.; Hendrickson, D. N.; Van Derveer, D. G.; Barefield, E. K. *J. Am. Chem. Soc.* **1979**, *101*, 906−917.
(28) Di Vaira, M.; Orioli, P. L. *Acta Crystallogr.* **1968**, *B24*, 1269−1272.
(29) Hagen, K. S. Personal communication.
(30) Ciampolini, M.; Speroni, G. P. *Inorg. Chem.* **1966**, *5*, 45−49.
(31) Di Vaira, M.; Orioli, P. L. *Inorg. Chem.* **1969**, *8*, 2729−2734.
(32) Briat, B.; Canit, J. C. *Mol. Phys.* **1983**, *48*, 33−61.
(33) Figgis, B. N.; Gerloch, M.; Mason, R. *Acta Crystallogr.* **1964**, *17*, 506−508.
(34) Lauher, J. W.; Ibers, J. A. *Inorg. Chem.* **1975**, *14*, 348−352.
(35) Ito, M.; Amagai, H.; Fukui, H.; Kitajima, N.; Moro-oka, Y. *Bull. Chem. Soc. Jpn.* **1996**, *69*, 1937−1945.
(36) Kitajima, N.; Moro-oka, Y. Unpublished results.
(37) Abbreviations: acac, acetylacetonate; Im, imidazole; $Me_5$dien, bis-(2-(dimethylamino)ethyl)methylamine; $Me_6$tren, tris(2-(dimethylamino)-ethyl)amine; MeEDTrA, methylethylenediaminetriacetate; L = HB(3,5-$i$Pr$_2$pz)$_3$, hydrotris(3,5-diisopropyl-1-pyrazolyl)borate; OAc, acetate; OBz, benzoate; OTf, $CF_3SO_3^-$; PMAH, 2-((*N*-(aminoethyl)amino)methyl)-4-(*N*-(2-(4-imidazolyl)ethyl)carbamoyl)-5-bromopyrimidine; PY5, 2,6-(bis(2-pyridyl)methoxymethane)pyridine; TMC, 1,4,8,11-tetramethyl-1,4,8,11-tetraazacyclotetradecane; trpn, 3,3′,3″-triaminotripropylamine.

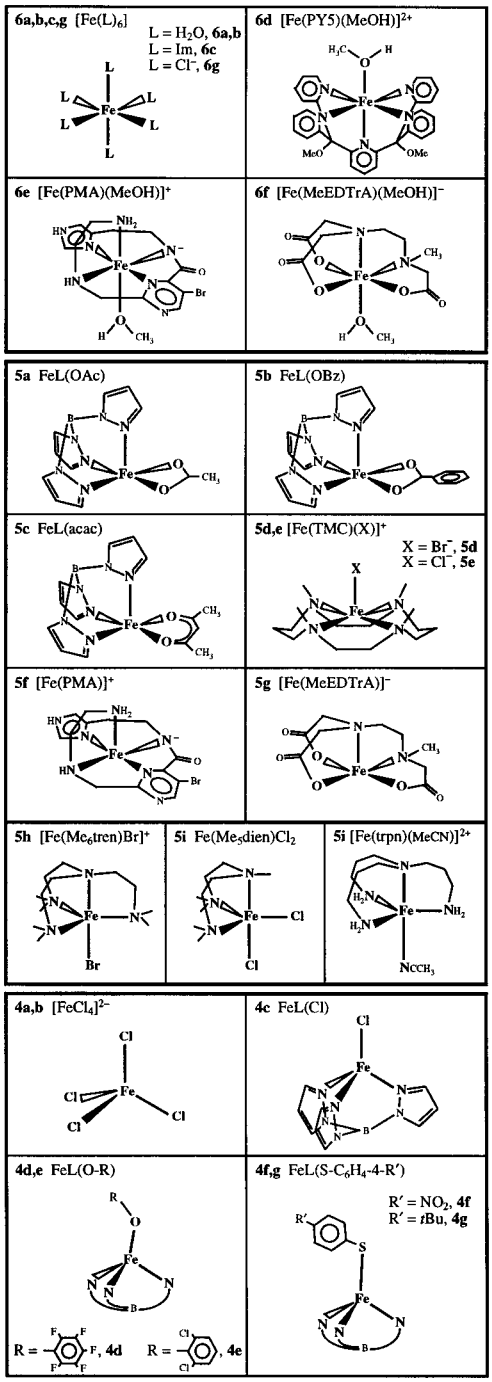


**Figure 1.** Structural representations of the 6-coordinate (top), 5-coordinate (middle), and 4-coordinate (bottom) ferrous models used in this study. The isopropyl groups of the ligand L in **5a**−**c** and **4c** have been omitted for clarity; L has been pictorially abbreviated for **4d**−**g**. Structural information is not yet available for **6f** and **5g**, but a suggested ligation is shown for the ligand system.[22]

of comparison for evaluating the nature of ferrous active sites in non-heme enzymes.

## Experimental Section

Commercial reagents were used without further purification: fluorolube (Wilmad), poly(dimethylsiloxane) (Aldrich), mineral oil (white, heavy; Mallinckrodt), glycerol-$d_3$ (98 atom % D; Cambridge Isotopes Laboratory), methyl-$d_3$ alcohol-$d$ (99.8 atom % D; Aldrich), ethyl-$d_5$ alcohol-$d$ (99+ atom % D; Aldrich), $D_2O$ (99.9 atom % D; Aldrich). The models $[Fe(H_2O)_6](NH_4)_2(SO_4)_2$ (MCB Manufacturing Chemists, Inc.) and $FeCl_2$ (anhydrous; Johnson Matthey Alfa) were obtained commercially. Other model complexes were prepared as previously described (see references in Table 1). All models except $[Fe(H_2O)_6](NH_4)_2(SO_4)_2$ and $[Fe(PY5)(MeOH)](OTf)_2$ are air-sensitive and were stored in an inert atmosphere.

All samples for spectroscopy were prepared under an inert atmosphere in a $N_2$-filled glovebox. Mulling agents were degassed prior to use by performing numerous freeze−pump−thaw cycles on an argon-gas Schlenk line. Crystalline samples were hand-ground into a fine powder using an agate mortar and pestle. Mulling agent (usually fluorolube, but poly(dimethylsiloxane) and mineral oil were also used) was added to the mortar and mixed with the powdered sample for 3−5 min. A drop of mull (∼200 $\mu$L) was placed on the center of an infrasil quartz disk and a second quartz disk laid on top. The two disks were placed on top of a neoprene spacer inside a copper MCD cell and held in position by a copper plate. Tightening down the copper plate spread the mull out evenly between the two quartz disks. Samples were inspected under an optical microscope to confirm that the microcrystalline mull was homogeneous and then immediately inserted into the MCD instrument under a high flow of helium gas.

For some models, the mull data showed ligand field transitions on top of an equally intense broad field-dependent background. In these cases, a more complete data set was collected on the solution form of the sample. Two of the models, [Fe(PMA)(MeOH)]Cl and Li[Fe(MeEDTrA)(MeOH)], were studied in both their 5C solid form and the 6C solvated form. In preparing solution samples, crystalline material was dissolved in previously degassed deuterated methanol ($[Fe(PY5)(MeOH)](OTf)_2$), deuterated ethanol ($[Fe(Im)_6]Cl_2$, [Fe(TMC)Br]Br, $[FeCl_4]^{2-}$), or $D_2O$ (Li[Fe(MeEDTrA)(MeOH)]) and mixed with ∼50−60% (vol %) degassed glycerol-$d_3$. [Fe(PMA)(MeOH)]Cl samples were prepared in a mixture of degassed methanol-$d_4$/ethanol-$d_6$ in a 1/4 ratio. Solutions were injected into a 0.3-cm-thick neoprene spacer sandwiched between two infrasil quartz disks and secured within the MCD cell by a copper plate. After removal from the glovebox, solution samples were either immediately frozen in liquid nitrogen or rapidly inserted into the MCD instrument under a high flow of helium gas.

NIR (600−2100 nm) MCD spectra were recorded on a Jasco J200D spectropolarimeter with a liquid nitrogen-cooled InSb detector and an Oxford Instruments SM4-7T superconducting magnet/cryostat or the upgraded SM4000-7T model, each capable of fields up to 7 T and temperatures from 1.6 to 100 K. Depolarization of the frozen MCD samples was determined to be <5% by comparing the CD spectra of a nickel (+)-tartrate solution placed before and after the sample. MCD spectra are corrected for the natural CD and zero-field baseline effects due to the optical quality of the frozen sample by subtracting the corresponding 0 T scan at each temperature. The baseline-corrected spectra were fit to Gaussian band shapes using a modified Levenberg/Marquardt constrained nonlinear least-squares fitting routine. Saturation magnetization data were normalized to the maximum observed intensity and fit as described in the text. Both the negative and positive ZFS models were applied to the VTVH MCD data in determining the best fit.

## Results and Analysis

**A. Ligand Field Spectra and Excited-State Splittings.** NIR MCD spectra were measured for seven 6C ferrous complexes with distorted octahedral geometry (see Figure 1, top): $[Fe(H_2O)_6](SiF_6)$, $[Fe(H_2O)_6](NH_4)_2(SO_4)_2$ (Tutton's salt), $[Fe(Im)_6]Cl_2$, $[Fe(PY5)(MeOH)](OTf)_2$, [Fe(PMA)(MeOH)]Cl, Li[Fe(MeEDTrA)(MeOH)], and $FeCl_2$. The hexaaquo ferrous complexes $[Fe(H_2O)_6](SiF_6)$ and $[Fe(H_2O)_6](NH_4)_2(SO_4)_2$ have similar structures, with the former having a trigonal and the latter a rhombic distortion of the iron center. The imidazole ligands in $[Fe(Im)_6]^{2+}$ are arranged in a nearly octahedral fashion, although there are no symmetry relations between any of the imidazole groups. $[Fe(PY5)(MeOH)]^{2+}$, which has five pyridines from the pentadentate PY5 ligand, has Fe−N bond lengths typical for high-spin ferrous sites (2.15−2.20 Å) and a contracted axis along the N−Fe−methanol direction with a 2.10 Å Fe−N bond and a 2.04 Å Fe−O bond. $[Fe(PMA)(MeOH)]^{+}$

**Table 1.** Ferrous Model Complexes and Their Structural Type

| coord no. | (key) | complex[37] | $Fe^{2+}$ ligands | approximate site geometry | structure ref |
|---|---|---|---|---|---|
| 6 | **6a** | $[Fe(H_2O)_6](SiF_6)$ | 6O | dist. $O_h$ (trigonal) | 14, 15 |
| | **6b** | $[Fe(H_2O)_6](NH_4)_2(SO_4)_2$ | 6O | dist. $O_h$ | 16 |
| | **6c** | $[Fe(Im)_6]Cl_2$ | 6N | dist. $O_h$ | 17, 18 |
| | **6d** | [Fe(PY5)(MeOH)](OTf)$_2$ | 5N, 1O | dist. $O_h$ | 19 |
| | **6e** | [Fe(PMA)(MeOH)]Cl | 5N, 1O | dist. $O_h$ | 20, 21 |
| | **6f** | Li[Fe(MeEDTrA)(MeOH)] | 2N, 3O, 1O' | dist. $O_h$ | 22 |
| | **6g** | $FeCl_2$ | 6Cl | dist. $O_h$ ($\sim D_{3d}$) | 23 |
| 5 | **5a** | FeL(OAc) | 3N, 2O | dist. square pyr. | 24 |
| | **5b** | FeL(OBz) | 3N, 2O | dist. square pyr. | 24 |
| | **5c** | FeL(acac) | 3N, 2O | dist. square pyr. | 25 |
| | **5d** | [Fe(TMC)Br]Br | 4N, 1Br | ~square pyr. | 26, 27 |
| | **5e** | [Fe(TMC)Cl](BF$_4$) | 4N, 1Cl | ~square pyr. | 26, 27 |
| | **5f** | [Fe(PMA)]Cl | 5N | ~square pyr. | 20, 21 |
| | **5g** | Li[Fe(MeEDTrA)] | 2N, 3O | ~square pyr. | 22 |
| | **5h** | [Fe(Me$_6$tren)Br]Br | 4N, 1Br | trig. bipyr. | 28 |
| | **5i** | Fe(Me$_5$dien)Cl$_2$ | 3N, 2Cl | dist. trig. bipyr. | 30, 31 |
| | **5j** | [Fe(trpn)(MeCN)](OTf)$_2$ | 4N, 1N' | ~trig. bipyr. | 29 |
| 4 | **4a** | $(FeCl_4)(NEt_4)$ | 4Cl | $T_d$ | 32, 33 |
| | **4b** | $Cs_3FeCl_5$ | 4Cl | dist. $T_d$ ($\sim D_{2d}$) | 34 |
| | **4c** | FeL(Cl) | 3N, 1Cl | dist. $T_d$ ($\sim C_{3v}$) | 35 |
| | **4d** | FeL(O-$C_6F_5$) | 3N, 1O | dist. $T_d$ | 35 |
| | **4e** | FeL(O-$C_6H_3$-2,6-$Cl_2$) | 3N, 1O | dist. $T_d$ | 36 |
| | **4f** | FeL(S-$C_6H_4$-4-$NO_2$) | 3N, 1S | dist. $T_d$ | 36 |
| | **4g** | FeL(S-$C_6H_4$-4-*t*Bu) | 3N, 1S | dist. $T_d$ | 36 |

**Table 2.** Excited-State Transition Energies and Ligand Field Splittings for 6-Coordinate Models

| | complex | method[a] | obsd | transitions[b,c] | 10*Dq*[b] | $\Delta^5E_g$[b] | ref |
|---|---|---|---|---|---|---|---|
| **6a** | $[Fe(H_2O)_6](SiF_6)$ | MCD | 9600 (+) | 10800 (+) | 10200 | 1200 | 7 |
| | | abs | 8400 | 10800 | 9600 | 2400 | 39 |
| **6b** | $[Fe(H_2O)_6](NH_4)_2(SO_4)_2$ | MCD | 9200 (+) | 10800 (+) | 10000 | 1600 | |
| | | abs | 8700 | 10300 | 9500 | 1600 | 39 |
| **6c** | $[Fe(Im)_6]Cl_2$ | MCD | 10500 (+) | 12500 (+) | 11500 | 2000 | |
| | | MCD[d] | 9500 (+) | 10800 (+) | 10150 | 1300 | |
| | | abs | 9800 | 11750 | 10775 | 1950 | 17 |
| **6d** | [Fe(PY5)(MeOH)](OTf)$_2$ | MCD | 11000 (+) | 13000 (+) | 12000 | 2000 | |
| | | MCD[d] | 11400 (+) | 12900 (+) | 12150 | 1500 | |
| **6e** | [Fe(PMA)(MeOH)]Cl | MCD[d] | 10100 (+) | 12200 (+) | 11150 | 2100 | 10 |
| **6f** | Li[Fe(MeEDTrA)(MeOH)] | MCD[d] | 9200 (+) | 11100 (+) | 10150 | 1900 | 38 |
| **6g** | $FeCl_2$ | MCD | 6700 (+) | 7400 (+) | 7050 | 700 | |
| | | abs | | ~7000 | ~7000 | | 40, 41 |
| | average[e] | | | | ~10200 | ~1800 | |

[a] MCD data collected at 1.6−5 K. [b] Values in $cm^{-1}$. [c] Signs of the MCD transitions are included. [d] Data taken on solution form of sample. [e] Excluding $FeCl_2$ data.

is a 6C complex designed to model the active site in bleomycin[20,21] and has mostly N ligation with the PMA ligand binding through primary and secondary amines, an imidazole, a pyrimidine, and a deprotonated amide. X-ray absorption spectroscopy studies[10] show typical Fe−N bond lengths and a short ~2.00 Å Fe−pyrimidine bond. [Fe(MeEDTrA)(MeOH)]$^-$ was synthesized to model the non-heme active site in phenylalanine hydroxylase[38] and has predominantly O ligands in a mixed oxygen and nitrogen distorted octahedral arrangement.[22] The iron center in $FeCl_2$ is surrounded by six Cl anions in a layered lattice so that the effective site symmetry is distorted octahedral ($\sim D_{3d}$).

Low-temperature MCD spectra for the 6C models are presented in Figure 2. (Gaussian resolutions are given in the Supporting Information.) Table 2 summarizes the observed d → d transition energies, 10*Dq* values, and $\Delta^5E_g$ splittings and compares these results to those from absorption spectroscopy where available. The two ferrous hexaaquo models have similar ligand field spectra (Figure 2, **6a,b**) and show additional weak spin-forbidden transitions to higher energy.[42] $[Fe(Im)_6]^{2+}$ has an MCD spectrum (**6c**) similar to that of the hexaaquo models, with the d → d bands shifted to slightly higher energy since imidazole is a stronger-field ligand than water. Ligand field transitions are observed at highest energy for [Fe(PY5)(MeOH)]$^{2+}$ (**6d**), which has five strong-field pyridine ligands; in fact, this complex can become low-spin rather easily by changing the nature of the sixth ligand.[43] The spectrum of [Fe(PMA)(MeOH)]$^+$ (**6e**) shows two transitions also to higher energy relative to the hexaaquo complexes which indicates a stronger ligand field at the iron center, likely due to the strong Fe−pyrimidine interaction. [Fe(MeEDTrA)(MeOH)]$^-$ shows spectral features (**6f**) similar to those of the hexaaquo models, as might be anticipated due to the largely O ligation. The d → d transitions for $FeCl_2$ are observed at ~7000 $cm^{-1}$ (**6g**) and are shifted to lower energy in accord with the weaker ligand field strength of Cl relative to N or O.[44] Thus it is found that

(38) Kasibhatla, B. T.; Loeb, K. E.; Westre, T. E.; Rodriguez, J. H.; Debrunner, P. G.; Hedman, B.; Hodgson, K. O.; Solomon, E. I.; Caradonna, J. P. Manuscript in preparation.

(39) Cotton, F. A.; Meyers, M. D. *J. Am. Chem. Soc.* **1960**, *82*, 5023−5026.

(40) Jones, G. D. *Phys. Rev.* **1967**, *155*, 259−261.

(41) Freeman, T. E.; Jones, G. D. *Phys. Rev.* **1969**, *182*, 411−415.

(42) Agnetta, G.; Garofano, T.; Palma-Vittorelli, M. B.; Palma, M. U. *Philos. Mag.* **1962**, *7*, 495−498.

(43) Jonas, R. T.; Stack, T. D. P. Personal communication.

(44) Lever, A. B. P. *Inorganic Electronic Spectroscopy*, 2nd ed.; Elsevier Science Publishing Co., Inc.: New York, 1984.

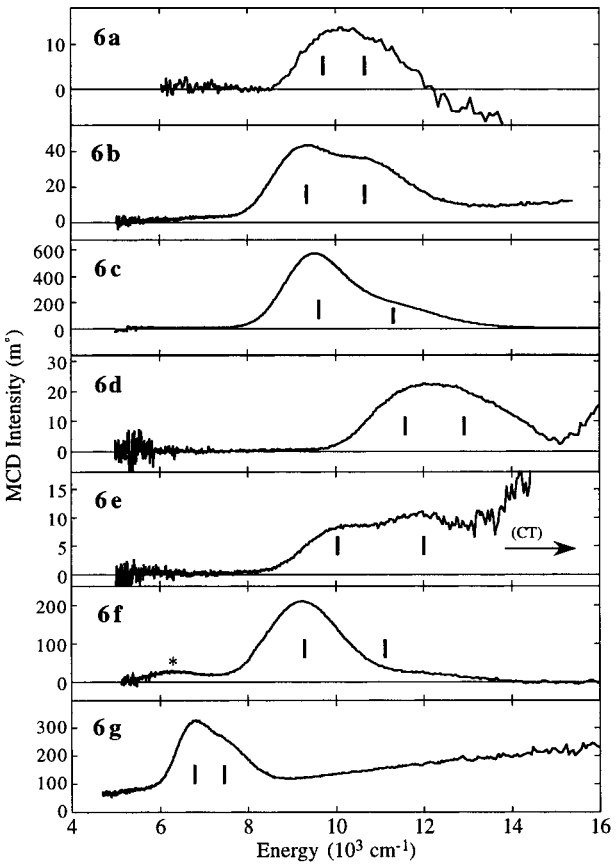


**Figure 2.** Low-temperature (1.6−5 K, 7 T) MCD spectra of 6-coordinate models: $[Fe(H_2O)_6](SiF_6)$ (**6a**), $[Fe(H_2O)_6](NH_4)_2(SO_4)_2$ (**6b**), $[Fe(Im)_6]^{2+}$ (**6c**), $[Fe(PY5)(MeOH)]^{2+}$ (**6d**), $[Fe(PMA)(MeOH)]^{+}$ (**6e**), $[Fe(MeEDTrA)(MeOH)]^{-}$ (**6f**), and $FeCl_2$ (**6g**). Ligand field transition energies are marked by bars (see Table 2). The negative feature to high energy in **6a** is a spin-forbidden transition;[42] the high-energy intensity marked as CT in **6e** is due to low-lying charge-transfer transitions.[10] An asterisk (*) indicates impurities in **6f** (residual starting material).

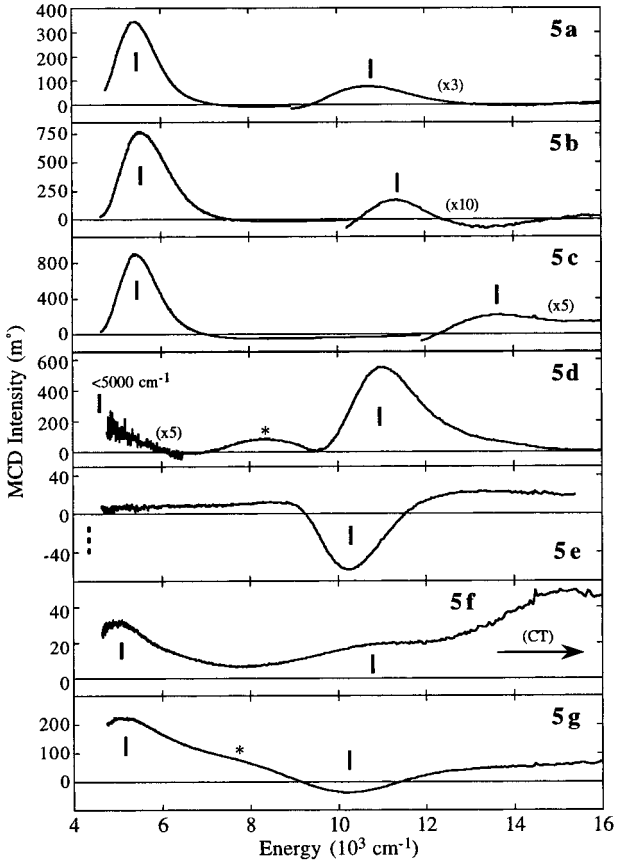


**Figure 3.** Low-temperature (1.6−5 K, 7 T) MCD spectra of 5-coordinate models with approximate square pyramidal geometry: FeL(OAc) (**5a**), FeL(OBz) (**5b**), FeL(acac) (**5c**), $[Fe(TMC)(Br)]^{+}$ (**5d**), $[Fe(TMC)(Cl)]^{+}$ (**5e**), $[Fe(PMA)]^{+}$ (**5f**), and $[Fe(MeEDTrA)]^{-}$ (**5g**). Ligand field transition energies are marked by bars (see Table 3). The high-energy intensity marked as CT in **5f** is due to low-lying charge-transfer transitions.[10] Asterisks (*) indicate impurities in **5d,g**.

6C ferrous complexes with N and O ligands show two features in the 10 000−12 000 $cm^{-1}$ region, with average values of $10Dq \approx 10\,200$ $cm^{-1}$ and $\Delta^5E_g \approx 1800$ $cm^{-1}$.

NIR MCD spectra were measured for seven 5C ferrous complexes with approximate square pyramidal geometry (see Figure 1, upper middle): FeL(OAc), FeL(OBz), FeL(acac), [Fe(TMC)Br]Br, $[Fe(TMC)Cl](BF_4)$, [Fe(PMA)]Cl, and Li[Fe(MeEDTrA)]. The first three are structurally similar with three equivalent N ligands and two O ligands from a bidentate acetate, benzoate, or acac group. One Fe−N bond is the axial direction with the two other nitrogens at nearly 90° and the oxygens completing the equatorial plane. The Fe−O bonds in FeL(OAc) and FeL(OBz) are inequivalent, with one bond at ∼2.23 Å and the other at ∼2.1 Å; in contrast, the Fe−O bonds in FeL(acac) are nearly equivalent and considerably shorter at ∼2.05 Å. The $[Fe(TMC)(X)]^{+}$ complexes contain four N ligands derived from the tetradentate TMC ligand and vary in the occupation of the fifth (axial) site. The N ligands are coplanar and the iron atom is slightly shifted out this equatorial plane toward the axial ligand. $[Fe(PMA)]^{+}$ and $[Fe(MeEDTrA)]^{-}$ are versions of the 6C models lacking the sixth solvent (methanol) ligand.

The low-temperature MCD spectra of the square pyramidal 5C complexes are presented in Figure 3, and the transition energies and splittings are summarized in Table 3 (**5a**−**g**). (Gaussian resolutions have been omitted since the d → d bands for the 5C models do not generally overlap and transition energies are readily identified.) FeL(OAc) (Figure 3, **5a**), FeL(OBz) (**5b**), and FeL(acac) (**5c**) show similar intense low-energy positive features at ∼5500 $cm^{-1}$ and a second much weaker transition at >10 000 $cm^{-1}$, which shifts to higher energy following the trend of OAc < OBz < acac. For weak-axial square pyramidal complexes, the highest-energy transition is to the $d_{x^2-y^2}$ orbital.[3] The observed trend reflects the increasing ligand field strength within the equatorial plane, particularly the short Fe−O bonds in FeL(acac), which drives up the energy of the $d_{x^2-y^2}$ orbital. The MCD spectrum of $[Fe(TMC)Br]^{+}$ (**5d**) shows a more intense high-energy feature centered at ∼11 000 $cm^{-1}$ and a weaker component which grows in at <5000 $cm^{-1}$. (The additional feature at ∼8500 $cm^{-1}$ is an impurity which displays VTVH MCD behavior quantitatively different than that of the band at ∼11 000 $cm^{-1}$ (vide infra).) Although the lower-energy transition is not observed for $[Fe(TMC)Cl]^{+}$ (**5e**), the highest-energy d → d transition is observed at ∼10 200 $cm^{-1}$, an energy lower than was found for $[Fe(TMC)Br]^{+}$. From the spectrochemical series, $Cl^{-}$ is expected to be a stronger-field ligand than $Br^{-}$.[44] Increasing the strength of the axial ligand from $Br^{-}$ to $Cl^{-}$ will shift the metal out of the equatorial plane and stabilize the $d_{x^2-y^2}$ orbital, lowering the energy of this transition for $[Fe(TMC)Cl]^{+}$. Both $[Fe(PMA)]^{+}$ (**5f**) and $[Fe(MeEDTrA)]^{-}$ (**5g**) have mixed N and O ligation and show two transitions at ∼5100 and ∼11 000 $cm^{-1}$, with the low-energy bands being more intense. Thus, in general, the square

(45) Ciampolini, M.; Nardi, N. *Inorg. Chem.* **1966**, *5*, 1150−1154.

**Table 3.** Excited-State Transition Energies and Ligand Field Splittings for 5-Coordinate Models

| | complex | method[a] | obsd | transitions[b,c] | $10Dq$[b] | $\Delta^5E_g$[b] | ref |
|---|---|---|---|---|---|---|---|
| **5a** | FeL(OAc) | MCD | 5500 (+) | 10700 (+) | 8100 | 5200 | |
| | | abs | ~5600 | ~10800 | 8200 | 5200 | |
| **5b** | FeL(OBz) | MCD | 5600 (+) | 11550 (+) | 8575 | 5950 | |
| | | abs | ~5600 | ~10800 | 8200 | 5200 | |
| **5c** | FeL(acac) | MCD | 5400 (+) | 13500 (+) | 9450 | 8100 | |
| **5d** | [Fe(TMC)Br]Br | MCD[d] | <5000 (+) | 11000 (+) | | >6000 | |
| | | MCD | n.o. | 11100 (+) | | >6000 | |
| **5e** | [Fe(TMC)Cl]($BF_4$) | MCD | n.o. | 10200 (−) | | >5000 | |
| **5f** | [Fe(PMA)]Cl | MCD | 5100 (+) | 11200 (+) | 8150 | 6100 | 10 |
| **5g** | Li[Fe(MeEDTrA)] | MCD | 5050 (+) | 10220 (−) | 7635 | 5170 | 38 |
| **5h** | [Fe($Me_6$tren)Br]Br | MCD | n.o. | 9500 (+) | | >5000 | |
| | | abs | 3800 | 9800 | | 6000 | 45 |
| **5i** | Fe($Me_5$dien)$Cl_2$ | MCD | n.o. | 8600 (−) | | >5000 | |
| | | abs | <4000 | 8400 | | >4500 | 30 |
| **5j** | [Fe(trpn)(MeCN)]($OTf)_2$ | MCD | n.o. | 11500 (+) | | >5000 | |
| | average | | | | | ~5700 | |

[a] MCD data collected at 1.6−5 K. [b] Values in $cm^{-1}$. [c] Signs of the MCD transitions are included. n.o. = not observed. [d] Data taken on solution form of sample.

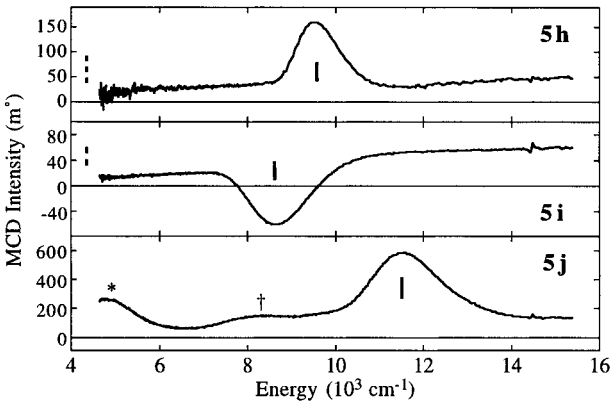


**Figure 4.** Low-temperature (1.6−5 K, 7 T) MCD spectra of 5-coordinate models with approximate trigonal bipyramidal geometry: [Fe($Me_6$tren)Br]$^+$ (**5h**), Fe($Me_5$dien)$Cl_2$ (**5i**), and [Fe(trpn)(MeCN)]$^{2+}$ (**5j**). Ligand field transition energies are marked by bars (see Table 3). For spectrum **5j**, an asterisk (*) marks a band due to a diamagnetic impurity, and a dagger (†) indicates a small paramagnetic impurity (see text).

pyramidal complexes show two ligand field transitions in the NIR region at >5000 and >10 000 $cm^{-1}$ with an average splitting of $\Delta^5E_g \approx 5700$ $cm^{-1}$.

The second group of 5C ferrous complexes studied have approximate trigonal bipyramidal geometry (see Figure 1, lower middle): [Fe($Me_6$tren)Br]Br, Fe($Me_5$dien)$Cl_2$, and [Fe(trpn)(MeCN)]($OTf)_2$. [Fe($Me_6$tren)Br]$^+$ has one axial and three equatorial N ligands in a tripod arrangement from the $Me_6$tren ligand, with Br occupying the other axial site; the metal ion lies on a crystallographic $C_3$ axis and has effective $C_{3v}$ site symmetry. [Fe(trpn)(MeCN)]$^{2+}$ is similar to the previous model but contains one additional carbon in the arms of the tetradentate tripod ligand, which causes a moderate degree of disorder in the crystal structure.[29] Fe($Me_5$dien)$Cl_2$ has only a partial tripod ligand providing one axial and two equatorial N ligands; Cl ligands occupy the remaining axial and equatorial sites to complete the coordination sphere.

Figure 4 shows the low-temperature NIR MCD spectra of these 5C complexes, and the transition energies and splittings are summarized in Table 3 (**5h**−**j**). [Fe($Me_6$tren)Br]$^+$ (Figure 4, **5h**) and Fe($Me_5$dien)$Cl_2$ (**5i**) show a single MCD transition at 9500 and 8600 $cm^{-1}$, respectively, in good agreement with the absorption spectra for these complexes. The absorption spectra indicate a second band to lower energy at <4000 $cm^{-1}$ for both models; however, these transitions are not observed in MCD due to the range of the instrument. Thus, the excited-state splitting for these complexes is large, >5000 $cm^{-1}$. The spectrum of [Fe(trpn)(MeCN)]$^{2+}$ (**5j**) shows three bands which are centered at ~5000, ~8500, and 11 500 $cm^{-1}$. The lowest-energy transition shows temperature-independent *B*-term behavior, rather than the usual temperature-dependent *C*-term behavior associated with high-spin ferrous sites (vide infra), indicating that this feature is due to a diamagnetic impurity. The spectra from different preparations of [Fe(trpn)(MeCN)]$^{2+}$ show different intensity ratios between the ~8500 and 11 500 $cm^{-1}$ bands, with the higher-energy band 5−10 times more intense. The VTVH MCD data at ~8500 $cm^{-1}$ fit to different ground-state parameters than for the 11 500 $cm^{-1}$ band (see section B), indicating different ground states and hence different species. Therefore, the weak feature at 8500 $cm^{-1}$ is likely due to a small paramagnetic impurity and the 11 500 $cm^{-1}$ band arises from the [Fe(trpn)(MeCN)]$^{2+}$ chromophore. This 11 500 $cm^{-1}$ band, which corresponds to the transition to the $d_{z^2}$ orbital, is at significantly higher energy than for the other trigonal bipyramidal models. This can be attributed to a stronger axial bond in [Fe(trpn)(MeCN)]$^{2+}$ compared to the relatively long axial bond in [Fe($Me_6$tren)Br]$^+$ (Fe−Br = 2.5 Å) which destabilizes the $d_{z^2}$ orbital. Therefore, while most trigonal bipyramidal ferrous models are weak-axial systems which show one ligand field transition at <10 000 $cm^{-1}$, strong-axial systems can show a band at >10 000 $cm^{-1}$. The second lower-energy ligand field transition for trigonal bipyramidal geometry is expected at <5000 $cm^{-1}$ and cannot be observed in the MCD spectra due to the instrument cutoff.

NIR MCD spectra were measured for seven 4C ferrous complexes (see Figure 1, bottom): [$FeCl_4$]($NEt_4$), $Cs_3FeCl_5$, FeL(Cl), FeL(O-$C_6F_5$), FeL(O-$C_6H_3$-2,6-$Cl_2$), FeL(S-$C_6H_4$-4-$NO_2$), and FeL(S-$C_6H_4$-4-*t*Bu). The first two models have tetrahedral geometries, with a $D_{2d}$ distortion of the [$FeCl_4$]$^{2-}$ center in $Cs_3FeCl_5$. The five FeL(X) compounds have similar structures, containing three N ligands with bond distances of ~2.00−2.13 Å. The models vary in the occupation and orientation of the fourth ligand site. FeL(Cl) has approximately $C_{3v}$ site symmetry with the 2.2 Å Fe−Cl bond ~1° off the normal to the plane of the three nitrogens. In FeL(O-$C_6F_5$), the Fe−O bond is contracted at 1.84 Å and oriented ~11° off the normal to the plane of the Ns. This angle increases to ~21° for FeL(O-$C_6H_3$-2,6-$Cl_2$), which has a similarly short 1.88 Å Fe−O bond, giving a much more distorted geometry for this complex. Both FeL(S-$C_6H_4$-4-R′) models have shorter Fe−N

**Table 4.** Excited-State Transition Energies and Ligand Field Splittings for 4-Coordinate Models

| | complex | method[a] | obsd | transitions[b,c] | 10*Dq*[b] | ES splitting[b] | ref |
|---|---|---|---|---|---|---|---|
| **4a** | $[FeCl_4](NEt_4)$ | MCD | <4700 (−) | | | | |
| | | MCD[d] | <4700 (−) | | | | |
| | | abs | 4060 | | ∼4000 | | 46 |
| **4b** | $Cs_3FeCl_5$ | MCD | <4700 (−) | | | | |
| **4c** | FeL(Cl) | MCD | 5930 (+) | 6650 (+) | 6290 | 720 | |
| **4d** | FeL(O-$C_6F_5$) | MCD | 6490 (+) | 7850 (+) | 7170 | 1360 | |
| **4e** | FeL(O-$C_6H_3$-2,6-$Cl_2$) | MCD | 6700 (+) | 9610 (+) | 8155 | 2910 | |
| **4f** | FeL(S-$C_6H_4$-4-$NO_2$) | MCD | 5590 (+) | 6600 (+) | 6095 | 1010 | |
| **4g** | FeL(S-$C_6H_4$-4-*t*Bu) | MCD | 5670 (+) | 7550 (+) | 6610 | 1880 | |
| | average[e] | | | | ∼7000 | ∼1600 | |

[a] MCD data collected at 1.6−5 K. [b] Values in $cm^{-1}$. [c] Signs of the MCD transitions are included. [d] Data taken on solution form of sample. [e] Excluding $[FeCl_4]^{2-}$ data.

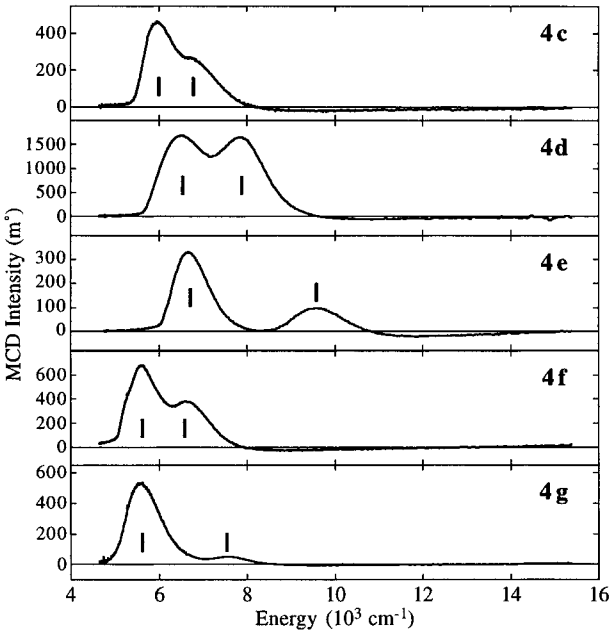


**Figure 5.** Low-temperature (1.6−5 K, 7 T) MCD spectra of 4-coordinate models: FeL(Cl) (**4c**), FeL(O-$C_6F_5$) (**4d**), FeL(O-$C_6H_3$-2,6-$Cl_2$) (**4e**), FeL(S-$C_6H_4$-4-$NO_2$) (**4f**), and FeL(S-$C_6H_4$-4-*t*Bu) (**4g**). Ligand field transition energies are marked by bars (see Table 4). Spectra of the $[FeCl_4]^{2-}$ models (**4a,b**) have been omitted since just the tails of the MCD transitions are observed due to the instrument cutoff at ∼4700 $cm^{-1}$.

bonds with the metal closer to the equatorial plane and ∼2.3 Å Fe−S bonds that are oriented ∼3° (R′ = $NO_2$) and ∼5° (R′ = *t*Bu) off the normal to the Ns plane.

The MCD transition energies and splittings for the 4C models are summarized in Table 4. (Gaussian resolutions are provided in the Supporting Information.) The MCD spectra of the $[FeCl_4]^{2-}$ models (not given) show the tail of their ligand field transitions at the low-energy cutoff of the instrument, <4700 $cm^{-1}$, and absorption spectra place this $^5T_2 \rightarrow {}^5E$ transition at ∼4000 $cm^{-1}$. The distorted 4C complexes with predominantly stronger-field N ligands show d → d transitions shifted to higher energy (Figure 5). The spectrum of FeL(Cl) (Figure 5, **4c**) shows two features centered at ∼6300 $cm^{-1}$ which are split by a small amount, ∼700 $cm^{-1}$. Replacing Cl with O causes 10*Dq* ($T_d$) to shift to higher energy, ∼7200 $cm^{-1}$ for FeL(O-$C_6F_5$) (**4d**) and ∼8200 $cm^{-1}$ for FeL(O-$C_6H_3$-2,6-$Cl_2$) (**4e**), as expected for the increased ligand field strength of O vs Cl. The splitting between the two bands has also increased relative to FeL(Cl) to ∼1360 $cm^{-1}$ for FeL(O-$C_6F_5$) and ∼2900 $cm^{-1}$ for FeL(O-$C_6H_3$-2,6-$Cl_2$). This excited-state splitting likely reflects the increased distortion of the site as the Fe−X angle to the normal of the Ns plane increases from ∼1° (Cl) to ∼11° (O-$C_6F_5$) to ∼21° (O-$C_6H_3$-2,6-$Cl_2$). The FeL(S-$C_6H_4$-4-R′) models (**4f,g**) have nearly identical low-energy bands at ∼5600 $cm^{-1}$ and a second transition at ∼6600 $cm^{-1}$ (R′ = $NO_2$) and ∼7550 $cm^{-1}$ (R′ = *t*Bu). Although the N−Fe−S angles are similar for the two complexes, the energy of the second transition is likely influenced by the substituent on the aromatic ring bound to the sulfur ligand. The higher 10*Dq* value for the FeL(O-R) models relative to the FeL(S-$C_6H_4$-4-R′) complexes indicates a strong ligand field at the iron site which is attributed to the significantly short ∼1.9 Å Fe−O bonds relative to the weaker Fe−S bonds. Thus the 4C ferrous complexes generally show one to two transitions centered at 10*Dq* ≈ 7000 $cm^{-1}$ and split by 700−3000 $cm^{-1}$.

One striking feature in the MCD spectra of the ferrous model complexes is the fact that the signs of the MCD transitions are mostly positive. The spectra for the 6C models show only positive MCD bands, as do all of those for the distorted 4C models. Although the entire low-energy band for $[FeCl_4]^{2-}$ is not observed, it appears that the sign of this MCD transition is negative. Of the 5C models studied, all of the MCD bands are positively signed except for the highest-energy ligand field transition for $[Fe(TMC)Cl]^+$ (**5e**), [Fe(MeEDTrA)]$^-$ (**5g**), and Fe($Me_5$dien)$Cl_2$ (**5i**).

**B. Saturation Magnetization and Ground-State Ligand Field Splittings.** At low temperatures, MCD spectra are dominated by *C*-terms, whose intensity derives from the differential population between Zeeman-split subcomponents of a degenerate ground state.[47,48] As the magnetic field (*H*) increases and/or the temperature (*T*) decreases, the population of the lowest-energy component grows and the MCD intensity increases until the ground-state population is maximized, at which point the intensity saturates. This saturation magnetization behavior is probed by measuring the MCD intensity at a range of fields and a series of fixed temperatures. VTVH MCD data for a representative ferrous model of each coordination type (**6b** for distorted octahedral, **5b** for square pyramidal, **5h** for trigonal bipyramidal, and **4c** for distorted tetrahedral) are shown in Figure 6. (The data for complexes **6c**,**d**, **5a**,**c**,**d**,**j**, and **4d**,**e**,**f**,**g** are shown in the Supporting Information.) For each example, the field or temperature dependence of the MCD spectrum is presented, and the VTVH MCD data collected at the indicated wavelengths have been normalized and plotted vs $\beta H/2kT$ and vs $1/kT$, where $\beta$ is the Bohr magneton and *k* is Boltzmann's

(46) Furlani, C.; Cervone, E.; Valenti, V. *J. Inorg. Nucl. Chem.* **1963**, *25*, 159−163.

(47) Buckingham, A. D.; Stephens, P. J. *Annu. Rev. Phys. Chem.* **1966**, *17*, 399−432.

(48) Piepho, S. B.; Schatz, P. N. *Group Theory in Spectroscopy with Applications to Magnetic Circular Dichroism*; John Wiley & Sons: New York, 1983.

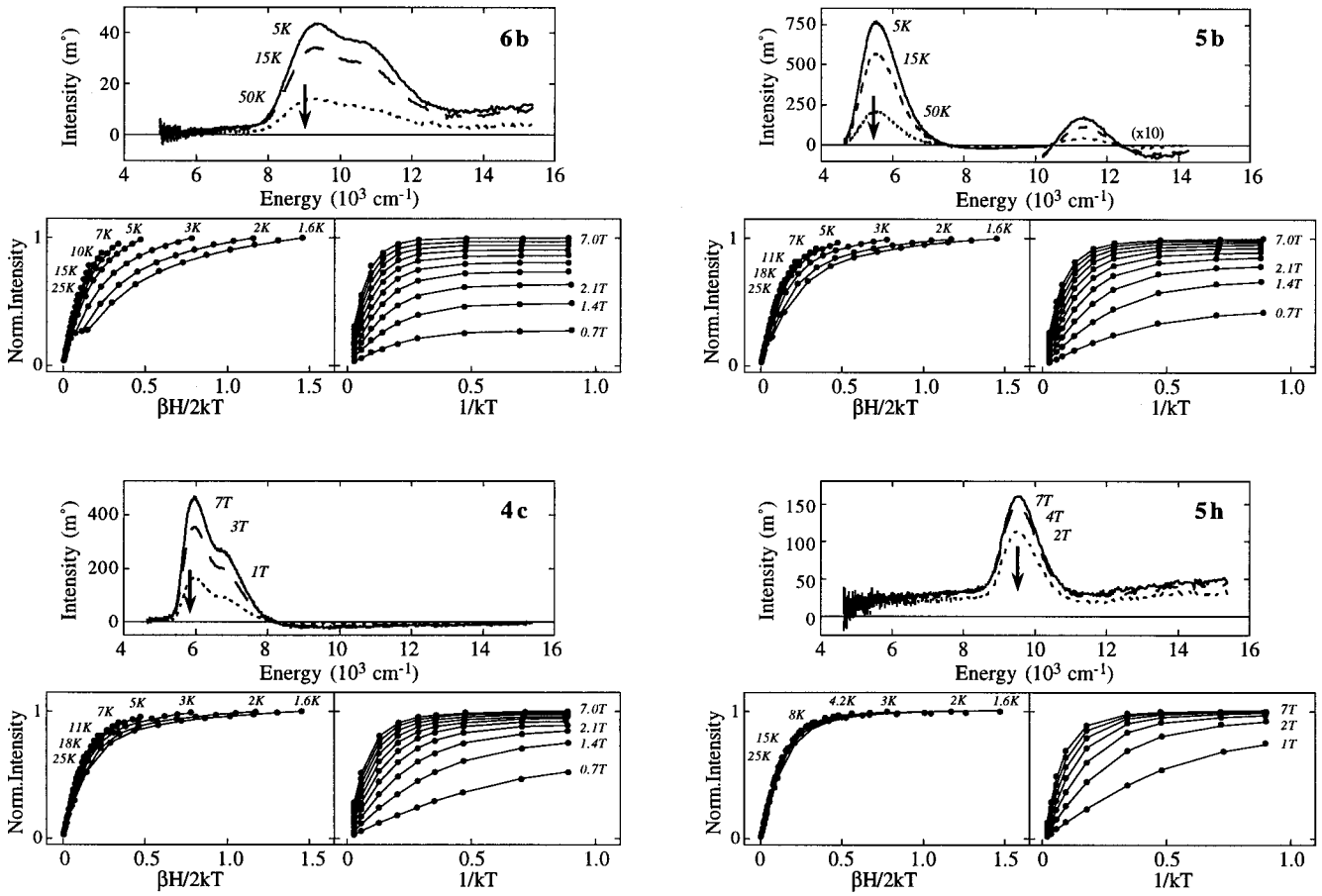


**Figure 6.** VTVH MCD data for selected ferrous models. Top left: $[Fe(H_2O)_6](NH_4)_2(SO_4)_2$ (**6b**), temperature dependence of the MCD spectrum at 7 T and VTVH MCD data (•) collected at 1100 nm (arrow). Top right: FeL(OBz) (**5b**), temperature dependence of the MCD spectrum at 7 T and VTVH MCD data (•) collected at 1800 nm (arrow). Bottom right: $[Fe(Me_6tren)Br]^+$ (**5h**), field dependence of the MCD spectrum at 4.2 K and VTVH MCD data (•) collected at 1050 nm (arrow). Bottom left: FeL(Cl) (**4c**), field dependence of the MCD spectrum at 5 K and VTVH MCD data (•) collected at 1740 nm (arrow). VTVH MCD data were collected at the indicated temperatures and at fields from 0 to 7 T in 0.7 T increments for **6b**, **5b**, and **4c** and in 1.0 T increments for **5h**. Fits (lines) to the VTVH MCD data were generated by the parameters in Table 5. Error bars are equal to or smaller than the symbol size used.

constant. The saturation magnetization data for the ferrous models, which are non-Kramers (integer spin) ions, display nested isotherms, that is the data plotted vs $\beta$H/2$kT$ do not superimpose. The data plotted vs 1/$kT$ in Figure 6 reveal that the saturated intensity increases nonlinearly with increasing field, indicating an unusual field dependence of the MCD intensity associated with the lowest component of the ground state. This behavior is interpreted in terms of the magnetic field dependence of the zero-field-split ground-state sublevels.

For systems with −ZFS ($D$ < 0), the non-Kramers $M_S = \pm 2$ doublet is lowest in energy. In the absence of a magnetic field, a rhombic distortion causes the doublet to split by an amount $\delta$ and mixes the wave functions to produce $|X\rangle = (|+2\rangle + |-2\rangle)/\sqrt{2}$ and $|Y\rangle = (|+2\rangle - |-2\rangle)/\sqrt{2}$ (Figure 7, left). When a magnetic field is applied, the components of the $M_S = \pm 2$ doublet are further split due to the Zeeman effect and the wave functions change in a nonlinear fashion, approaching pure $|+2\rangle$ and $|-2\rangle$ at high magnetic field, as shown in Figure 7 (left). It is this nonlinear field dependence of the wave functions that accounts for the observed nested saturation magnetization behavior, and simulations show that the magnitude of $\delta$ is directly proportional to the degree of nesting.[3] For +ZFS systems ($D$ > 0), the singlet $M_S = 0$ sublevel is lowest in energy with the $M_S = \pm 1$ doublet at $D$ cm$^{-1}$ above (Figure 7, right). When a magnetic field is applied parallel to the molecular $z$-axis, the energy of the ground-state $M_S = 0$ level is independent of field; thus, one expects no MCD intensity at low temperatures when only the $C$-term-inactive $M_S = 0$ sublevel is populated and nonzero $C$-term intensity at higher temperatures as the $M_S = \pm 1$ doublet becomes thermally populated. However, this type of behavior is not observed in the VTVH MCD data collected for 19 ferrous models complexes. When a magnetic field is

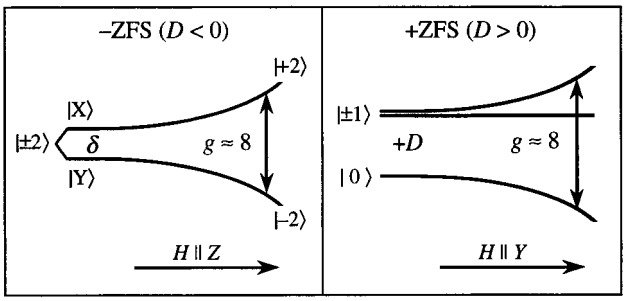


**Figure 7.** Zeeman splittings of the ground-state sublevels of an $S = 2$ non-Kramers system. For −ZFS (left), the $M_S = \pm 2$ components are split by a rhombic distortion ($\delta$) into the wave functions $|X\rangle = (|+2\rangle + |-2\rangle)/\sqrt{2}$ and $|Y\rangle = (|+2\rangle - |-2\rangle)/\sqrt{2}$; application of a magnetic field further splits the doublet with a $g \approx 8$ and causes the wave functions to mix in a nonlinear fashion. For +ZFS (right), the Zeeman effect with $H \perp Z$ couples the $M_S = 0$ and one component of the $M_S = \pm 1$ with a $g \approx 8$, producing a temperature-dependent nonlinear $B$-term. The effective ground-state splitting is expected to be larger for +ZFS than for −ZFS.

**Table 5.** VTVH MCD Fitting Parameters and Ground-State Spin-Hamiltonian and Ligand Field Parameters for $Fe^{2+}$ Models

| | complex | $\delta^a$ | $g_{\|\|}$ | $M_z/M_{xy}{}^b$ | *B*-term[c] (%) | $E_S{}^d$ | $D^e$ | $E^e$ | $\|E/D\|$ | $\Delta^a$ | $\|V\|^a$ | $\|V/2\Delta\|$ | ref |
|---|---|---|---|---|---|---|---|---|---|---|---|---|---|
| **6a** | $[Fe(H_2O)_6](SiF_6)$ | 10.0 | 8 | — | <1 | 11 | +12.0 | 0.7 | 0.06 | +500 | 80 | 0.08 | 7 |
| **6b** | $[Fe(H_2O)_6](NH_4)_2(SO_4)_2$ | 6.7 | 8.7 | — | 0.8 | 38 | — | — | — | 200 | 130 | 0.33 | |
| **6c** | $[Fe(Im)_6]Cl_2{}^f$ | 4.6 | 9.1 | −0.15 | 1.1 | 26 | — | — | — | −500 | 300 | 0.30 | |
| **6d** | [Fe(PY5)(MeOH)](OTf)$_2{}^f$ | 3.3 | 8.7 | −0.09 | 0.7 | 23 | — | — | — | 1000 | 670 | 0.33 | |
| **6e** | [Fe(PMA)(MeOH)]Cl$^f$ | 2.4 | 9.0 | — | 0.2 | — | — | — | — | −950 | 450 | 0.24 | 10 |
| **6f** | Li[Fe(MeEDTrA)(MeOH)]$^f$ | 4.4 | 9.3 | −0.7 | — | 30 | — | — | — | −400 | 180 | 0.22 | 38 |
| **5a** | FeL(OAc) | 4.0 | 8.7 | — | 1.0 | 21 | — | — | — | 800 | 530 | 0.33 | |
| **5b** | FeL(OBz) | 3.5 | 8.8 | −0.12 | 0.5 | 40 | — | — | — | 800 | 530 | 0.33 | |
| **5c** | FeL(acac) | 0.6 | 9.3 | −0.09 | 0.3 | 44 | — | — | — | −2000 | 320 | 0.08 | |
| **5d** | [Fe(TMC)Br]Br$^f$ | 1.0 | 9.0 | — | 0.7 | 40 | — | — | — | −1700 | 550 | 0.16 | |
| **5f** | [Fe(PMA)]Cl | 3.3 | 8.5 | — | 4.7 | — | — | — | — | 900 | 600 | 0.33 | 10 |
| **5g** | Li[Fe(MeEDTrA)] | 4.0 | 8 | — | 4.8 | 10 | +7.3 | 1.3 | 0.18 | +1000 | 440 | 0.22 | 38, 53 |
| **5h** | [Fe($Me_6$tren)Br]Br | 1.5 | 8.6 | — | 0.1 | 40 | (−*D*) | | | | | | |
| **5j** | [Fe(trpn)(MeCN)](OTf)$_2$ | 1.4 | 9.0 | — | 0.3 | 44 | (−*D*) | | | | | | |
| **4c** | FeL(Cl) | 2.0 | 8.9 | −0.15 | 0.6 | 52 | −20.8 | 3.8 | 0.18 | | | | |
| **4d** | FeL(O-$C_6F_5$) | 1.3 | 8.8 | — | 0.4 | 36 | −14.3 | 2.5 | 0.18 | | | | |
| **4e** | FeL(O-$C_6H_3$-2,6-$Cl_2$) | 1.2 | 8.5 | — | 0.5 | 25 | −10.2 | 2.0 | 0.20 | | | | |
| **4f** | FeL(S-$C_6H_4$-4-$NO_2$) | 6.2 | 8 | — | 0.3 | 19 | +12.5 | 2.7 | 0.21 | | | | |
| **4g** | FeL(S-$C_6H_4$-4-*t*Bu) | 6.8 | 8 | — | 0.6 | 16 | +11.9 | 2.0 | 0.17 | | | | |

[a] Values in $cm^{-1}$. [b] Value of $M_z/M_{xy}$ with $g_\perp$ fixed at 1.0; *z*-polarization has been included only if the fit quality significantly improved. [c] Reported as a percentage of the *C*-term intensity scaling factor $A_{satlim}$. [d] Energy of a singlet excited state (in $cm^{-1}$) above the centered energy of the ground-state doublet. [e] *D* and *E* ($cm^{-1}$) obtained using an $S = 2$ spin Hamiltonian.[52] [f] Data taken on solution form of sample.

applied perpendicular to *Z*, the $M_S = 0$ and $M_S = \pm 1$ sublevels interact through an off-axis Zeeman effect,[3] as shown for the case of $H||Y$ in Figure 7 (right). The $M_S = 0$ and one partner of the $M_S = \pm 1$ act as a pseudo-doublet with a $g \approx 8$, while the other partner of $M_S = \pm 1$ is nearly independent of field and can be approximated as a *C*-term-inactive singlet excited state (see Figure 7, right). The predicted VTVH MCD behavior for this "three-level model" is qualitatively similar to that of −ZFS with very large $\delta$, since the ground-state ZFS is now *D* $cm^{-1}$ ($2(D^2 + 3E^2)^{1/2} - D - 3E$ $cm^{-1}$ with rhombic ZFS), which is generally much larger than $\delta$.[3,7] Thus analysis of the VTVH MCD data allows one to distinguish the sign of the ZFS: +ZFS systems are readily recognized by the large splitting of the ground-state doublet combined with the presence of a low-lying *C*-term-silent singlet excited state.

Quantitative analysis of the VTVH MCD data (intensity, field, temperature) for ferrous systems allows one to extract ground-state sublevel splittings and effective *g* values, as well as to determine the polarization of a transition. The MCD *C*-term orientation averaged intensity expression for a non-Kramers doublet ground state with *xy*-polarized transitions has been described previously.[5] This equation has recently been expanded to include +ZFS ground states.[3,7] We have now derived a closed-form *C*-term intensity expression for non-Kramers systems with both *xy*- and *z*-polarized transitions, analogous to the equation developed for Kramers systems.[49,50] The complete non-Kramers MCD intensity expression including *z*-polarization and singlet and doublet excited states, along with linear, temperature-independent *B*-terms is given in eq 1. (The

$$\Delta\varepsilon = \sum_{i,\text{doublets}} \left\{ A_{\text{satlim}i} \int_0^{\pi/2} \left( g_{\|i} \cos^2\theta - \sqrt{2}\left(\frac{M_z}{M_{xy}}\right)_i g_{\perp i} \sin^2\theta \right) \frac{\beta H}{\Gamma_i} \alpha_i \sin\theta \, d\theta \right\} + \sum_{i,\text{doublets}} B_i H \gamma_i + \sum_{m,\text{singlets}} B_m H \eta_m \quad (1)$$

where $\Gamma_i = \sqrt{\delta_i^2 + (g_{\|i}\beta H\cos\theta)^2 + (g_{\perp i}\beta H\sin\theta)^2}$

$$\alpha_i = \frac{\left(e^{-(E_i - \Gamma_i/2)/kT} - e^{-(E_i + \Gamma_i/2)/kT}\right)}{\sum_{j,\text{doublets}} \left(e^{-(E_j - \Gamma_j/2)/kT} + e^{-(E_j + \Gamma_j/2)/kT}\right) + \sum_{n,\text{singlets}} \left(e^{-E_n/kT}\right)}$$

$$\gamma_i = \frac{\left(e^{-(E_i - \delta_i/2)/kT} + e^{-(E_i + \delta_i/2)/kT}\right)}{\sum_{j,\text{doublets}} \left(e^{-(E_j - \delta_j/2)/kT} + e^{-(E_j + \delta_j/2)/kT}\right) + \sum_{n,\text{singlets}} \left(e^{-E_n/kT}\right)}$$

$$\eta_m = \frac{\left(e^{-E_m/kT}\right)}{\sum_{j,\text{doublets}} \left(e^{-(E_j - \delta_j/2)/kT} + e^{-(E_j + \delta_j/2)/kT}\right) + \sum_{n,\text{singlets}} \left(e^{-E_n/kT}\right)}$$

derivation is included in the Supporting Information.) $\theta$ is the angle between the magnetic field and the molecular *z* axis, $A_{\text{satlim}i}$ is the *C*-term intensity scaling factor, $g_{\perp i} = g_{x,y}$ is fixed at either 0 (no *z*-polarization) or 1 (including *z*-polarization),[3] $(M_z/M_{xy})_i$ is the polarization ratio, $B_{i/m}$ is the *B*-term, and $E_{i/m}$ is the energy of each doublet *i* and each singlet *m* ($E_0 \equiv 0$ $cm^{-1}$); $\alpha_i$, $\gamma_i$, and $\eta_m$ are Boltzmann population terms.[51] For systems with −ZFS, $\delta$ is the spitting of the $M_S = \pm 2$ doublet, and for +ZFS systems, "$\delta$" $= 2(D^2 + 3E^2)^{1/2} - D - 3E$ is the splitting of $M_S = 0$ and one component of $M_S = \pm 1$ sublevels.

The complete MCD intensity expression in eq 1 has been applied to the saturation magnetization data for the ferrous models to extract ground-state spin-Hamiltonian parameters ($\delta$ and $g_{\|}$ for −ZFS and *D* and *E* for +ZFS[52]), and the results are given in Table 5. Contributions from linear, temperature-independent *B*-terms are generally small, less than ∼1%, and most of the data for the models listed in Table 5 are well described by the −ZFS splitting model for *C*-term intensity. The data for four complexes are fit by the +ZFS three-level model: $[Fe(H_2O)_6](SiF_6)$, which is known to have +ZFS,[54−56] $[Fe(MeEDTrA)]^-$, and the two FeL(S-$C_6H_4$-4-R′) models (**4f,g**).

(49) Schatz, P. N.; Mowery, R. L.; Krausz, E. R. *Mol. Phys.* **1978**, *35*, 1537−1557.

(50) Bennett, D. E.; Johnson, M. K. *Biochim. Biophys. Acta* **1987**, *911*, 71−80.

(51) Note that the Boltzmann factors for the *B*-terms differ from that for the *C*-term because field-induced mixing is much greater for perpendicular fields; therefore, the Zeeman splitting will be governed by $g_\perp$, which is very small for $S = 2$ systems (see ref 3).

(52) For a +ZFS system, $E = (E_S - \delta/2)/6$ and $+D = (\delta/3) + E + {}^2/_3[\delta^2 + 6\delta E]^{1/2}$, where $\delta$ is the zero-field splitting of the pseudodoublet ground state and $E_S$ is the energy of the singlet excited state using the three-level model. For a −ZFS system, *D* and *E* are calculated from $E = (\delta/6) + {}^1/_3[(\delta^2/2 + \delta E_S]^{1/2}$ and $-D = E + (E_S/3) - (\delta/6)$, where $\delta$ is the rhombic ZFS of the $M_S = \pm 2$ ground state and $E_S$ is the energy of a singlet excited state used to approximate the lower-energy component of the $M_S = \pm 1$ excited state.

(53) These data have been refit from the original reference (ref 38) using the +ZFS model and the updated fitting results are shown here.

(54) Jackson, L. C. *Philos. Mag.* **1959**, *4*, 269−272.

**Scheme 1**

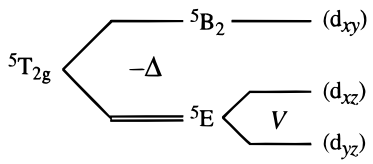


The results in Table 5 show relatively small polarization ratios, indicating that the ferrous d → d transitions are primarily *xy*-polarized. Although small, *z*-polarization contributions are important to include since they affect the magnitude of $g_{||}$ and often greatly improve the goodness of fit. The $g_{||}$ values obtained fall in a narrow range of 8.0−9.3. Error analysis of the fits and simulations[3] show that the VTVH MCD data are most sensitive to the value of $\delta$, which ranges from <1 to ∼10 $cm^{-1}$ (the latter for +ZFS).

The value of $\delta$ is found to be larger for 6C complexes (Table 5, top), generally $\delta > 4$ $cm^{-1}$, than for 5C complexes (Table 5, middle), correlating with the larger nesting observed experimentally for 6C relative to 5C models (Figure 6). The $\delta$ values for the $[Fe(H_2O)_6]^{2+}$ complexes obtained through the VTVH MCD analysis agree with ground-state splittings determined by far-IR spectroscopies: $\delta = 9.9$ $cm^{-1}$ for $[Fe(H_2O)_6](SiF_6)$[55] and $\delta = 6.4-6.7$ $cm^{-1}$ for $[Fe(H_2O)_6](NH_4)_2(SO_4)_2$.[57] There are two 6C models which deviate from the general trend of $\delta > 4$ $cm^{-1}$, both of which have at least one strong-field ligand at the ferrous site: $[Fe(PMA)(MeOH)]^+$, which has a short Fe−pyrimidine bond, and $[Fe(PY5)(MeOH)]^{2+}$, which has five pyridine ligands. In contrast to the large $\delta$ values observed for the 6C models, the 5C complexes show smaller ground-state splittings with $\delta < 4$ $cm^{-1}$. Four of the square pyramidal complexes have $\delta$ values in the 3−4 $cm^{-1}$ range, while two show much smaller values, $\delta = 0.6$ $cm^{-1}$ for FeL(acac) and $\delta = 1.0$ $cm^{-1}$ for $[Fe(TMC)Br]^+$. All of the trigonal bipyramidal 5C models were found to have small $\delta$ values, $\delta < 2$ $cm^{-1}$. The 4C models (Table 5, bottom) show either a small degree of nesting and −ZFS ($\delta < 2$ $cm^{-1}$) or rather large nesting ($\delta >$ 6 $cm^{-1}$) and +ZFS ($D \approx +12$ $cm^{-1}$). The larger $\delta$ values are found for the two FeL(S-$C_6H_4$-4-R′) models, while small $\delta$ values are seen for FeL(Cl) and both FeL(O-R) models, which have strong axial Fe−X bonds.

For the 6C and square pyramidal 5C complexes, the ground-state spin-Hamiltonian parameters obtained from the saturation magnetization analysis can be used to determine the orbital splittings of the $^5T_{2g}$ ground state. The triply orbitally degenerate $^5T_{2g}$ state is split by an axial ZFS distortion, $\Delta \equiv E(d_{xz,yz}) - E(d_{xy})$, and a rhombic distortion, $V \equiv E(d_{xz}) - E(d_{yz})$, as depicted in Scheme 1. When $\Delta$ is negative, the $^5E$ ($d_{xz}$,$d_{yz}$) state is lowest, indicating a weak axial direction which corresponds to −ZFS; conversely, a positive value of $\Delta$ indicates a strong axial system and +ZFS. Because the $^5T_{2g}$ state has both spin and orbital degeneracy, a spin Hamiltonian is not adequate to describe the sublevel splittings. Instead, a $^5T_{2g}$ Hamiltonian[3,5] must be used which includes spin−orbit coupling ($\lambda$) along with axial and rhombic ZFS and Zeeman effects, as given in eq 2.[58]

$$\hat{\mathcal{H}}(^5T_{2g}) = \lambda(\vec{L}\cdot\vec{S}) + \Delta\left\{\hat{L}_z^2 - \tfrac{1}{3}L(L+1)\right\} + \tfrac{1}{2}V(\hat{L}_x^2 - \hat{L}_y^2) + \beta\left\{(\hat{L}_x + 2\hat{S}_x)H_x + (\hat{L}_y + 2\hat{S}_y)H_y + (\hat{L}_z + 2\hat{S}_z)H_z\right\} \quad (2)$$

For systems with −ZFS, solutions of eq 2 are used to obtain graphs which relate $\delta$ and $g_{||}$ to the ligand field splitting parameters $-\Delta$ and $|V/2\Delta|$.[3,5] From these results, the effective $g_{||}$ value is expected to fall between 8 and 10 and $\delta$ is limited to $\leq 7$ $cm^{-1}$. For systems with +ZFS, the VTVH MCD fit results are used to obtain $+D$ and $|E|$, which in turn relate to $+\Delta$ and $V$. (See ref 3 for further details.)

This methodology has been applied to the 6C and 5C ferrous model complexes to obtain ground-state $t_{2g}$ orbital splittings, which are also included in Table 5. The sign of the ZFS is given unless the system is at the rhombic limit ($|V/2\Delta| = 0.33$). In general, the 6C complexes, which have large $\delta$ values, show a small splitting of the $t_{2g}$ orbitals regardless of the sign of the ZFS, $|\Delta| < 500$ $cm^{-1}$. Exceptions occur for [Fe(PMA)-(MeOH)]$^+$ and $[Fe(PY5)(MeOH)]^{2+}$, which have large $\Delta$ values, corresponding with the unusually small $\delta$ values. Conversely, the square pyramidal 5C complexes, which have smaller $\delta$ values, show larger $t_{2g}$ orbital splittings, $|\Delta| > 800$ $cm^{-1}$. The magnitude of $-\Delta$ is largest for FeL(acac) and $[Fe(TMC)Br]^+$, which have axial splitting patterns (small $|V/2\Delta|$ values), and smaller for the remaining square pyramidal models which have rhombic splitting patterns ($|V/2\Delta| \approx 0.33$).

For trigonal bipyramidal 5C ferrous sites with $C_{3v}$ symmetry, the orbital ground state is the doubly degenerate $^5E$ ($d_{xz}$,$d_{yz}$) state, with the $^5E$ ($d_{xy}$,$d_{x^2-y^2}$) and $^5A_1$ ($d_{z^2}$) states above, corresponding to −ZFS.[59,60] Experimentally, the VTVH MCD data for trigonal bipyramidal complexes are well described by the −ZFS non-Kramers doublet model and $\delta$ values are small, $\delta < 2$ $cm^{-1}$. While $\delta$ is a measure of the rhombic ZFS of the site and increases with increasing rhombicity, the origin of the small magnitude of $\delta$ for the trigonal bipyramidal case lies in the spin−orbit coupling interactions. From ref 3, in-state spin−orbit coupling within the $^5E$ ($d_{xz}$,$d_{yz}$) ground state splits the sublevels into five doublets, and a rhombic distortion further splits these into two sets of five, the lowest-energy set having a doublet−doublet−singlet (negative ZFS) pattern. Out-of-state spin−orbit coupling from the ground state to both the $^5E$ and $^5A_1$ excited states removes the degeneracy of the lowest-energy non-Kramers doublet so that these two components are split by a small amount, $\delta$. Because the states involved in out-of-state spin−orbit coupling with the ground state are at higher energy for trigonal bipyramidal complexes (generally ∼3000 and ∼9000 $cm^{-1}$)[44,61] than for square pyramidal complexes ($|\Delta| \approx$ 800−2000 $cm^{-1}$), this effect is calculated to be small, and thus $\delta$ is generally smaller for trigonal bipyramidal than for square pyramidal geometry.

In the case of 4C geometry, the $^5E$ ($d_{x^2-y^2}$, $d_{z^2}$) state is lowest in energy with the triply degenerate $^5T_2$ ($d_{xz}$, $d_{yz}$, $d_{xy}$) state at $10Dq$ ($T_d$) above. Because the $^5E$ ($d_{x^2-y^2}$, $d_{z^2}$) ground state has no orbital angular momentum, an $S = 2$ spin Hamiltonian[62] is appropriate to describe the sublevel splittings. From the values of $D$ in Table 5, both −ZFS and +ZFS ground states are observed experimentally for the 4C models. In the case of tetragonally distorted sites, the sign of the ZFS corresponds to an elongation or a compression along $z$ via a $D_{2d}$ distortion pathway: elongation produces a $d_{x^2-y^2}$ ground state and −ZFS and compression gives a $d_{z^2}$ ground state and +ZFS.[63] Most

(55) Champion, P. M.; Sievers, A. J. *J. Chem. Phys.* **1977**, *66*, 1819−1825.
(56) Gnezdilov, V. P.; Eremenko, V. V.; Peschanskii, A. V.; Fomin, V. I. *Fiz. Nizk. Temp. (Kiev)* **1991**, *17*, 253−258.
(57) Doerfler, R.; Allan, G. R.; Davis, B. W.; Pidgeon, C. R.; Vass, A. *J. Phys. C: Solid State Phys.* **1986**, *19*, 3005−3011.
(58) There is a typographical error in the earlier references for this equation (refs 3 and 5).
(59) Furlani, C. *Coord. Chem. Rev.* **1968**, *3*, 141−167.
(60) Wood, J. S. *Prog. Inorg. Chem.* **1972**, *16*, 277−486.
(61) Ciampolini, M. *Struct. Bonding* **1969**, *6*, 52−93.
(62) Abragam, A.; Bleaney, B. *Electron Paramagnetic Resonance of Transition Ions*; Dover Publications: New York, 1986.
(63) Varret, F.; Hartmann-Boutron, F. *Ann. Phys.* **1968**, *3*, 157−168.

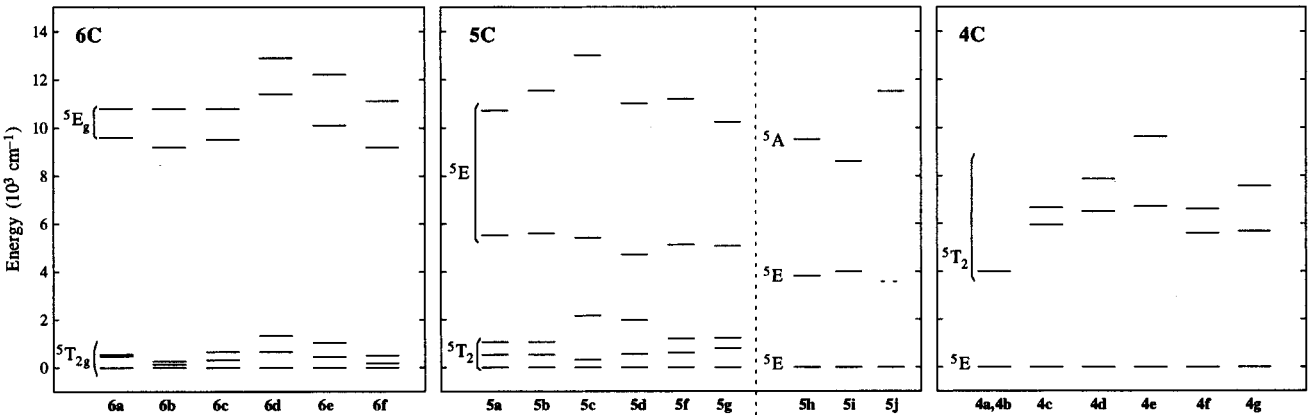


**Figure 8.** Experimental d-orbital energy level diagrams for 6C (left), 5C (middle), and 4C (right) models obtained through combining the excited-state transition energies and the ground-state ligand field analysis results from Table 5. (See Table 1 for compound names.) The $^5$E ground state for trigonal bipyramidal 5C and distorted tetrahedral 4C sites are also split (by $<1000$ cm$^{-1}$ from ligand field calculations); however, these splittings are not indicated as they are not determined from experiment.

of the 4C models in this study have trigonal distortions arising from the presence of one unique strong or weak ligand which defines the trigonal axis: FeL(Cl) (**4c**) and the FeL(O-R) complexes (**4d,e**) have strong axial interactions and $-$ZFS experimentally, while the FeL(S-$C_6H_4$-4-R′) models (**4f,g**) have weaker axial strengths and $+$ZFS. From ligand field calculations, application of a strong-axial trigonal distortion to tetrahedral geometry does not remove the degeneracy of the $^5$E ground state, as expected from group theory, but the wave function descriptions change, approaching ($d_{x^2-y^2}$, $d_{xy}$) due to the increased interaction along $z'$ (the prime indicates quantization along the trigonal axis). When a small rhombic perturbation as is appropriate for these 4C models is applied, the ground-state orbital degeneracy is lifted. Inclusion of spin$-$orbit coupling over all quintet states in the strong-axial case splits the $M_S$ sublevels so that an isolated doublet is lowest in energy with primarily $M_S = \pm 2$ character. This corresponds to $-$ZFS as is found experimentally for the strong-axial models, **4c**$-$**e**. Application of a weak-axial trigonal distortion shifts the $^5$E ground-state wave function descriptions toward ($d_{xz}$, $d_{yz}$) due to a stabilization along $z'$. Inclusion of a small rhombic perturbation and second-order spin$-$orbit coupling (to the $^5T_2$ low-symmetry-split excited-state components) produces a ground-state splitting pattern in which the two lowest-energy sublevels are split by a large amount with a third sublevel close in energy. Rotation of the $\tilde{\mathbf{D}}$ tensor to be along $y'$ shows that the lowest two sublevels act as an $M_S = \pm 2$ pseudododoublet. This larger splitting and off-axis field behavior corresponds to $+$ZFS and correlates with the experimental data for the weak-axial FeL(S-$C_6H_4$-4-R′) models. Thus, the sign of the ZFS for trigonally distorted 4C ferrous sites is correlated with the strength of the axial interaction and provides information about the nature of the ground-state orbital which contains the redox-active electron.

## Discussion

Ferrous active sites have previously been the least spectroscopically accessible form of the non-heme iron enzymes, yet the study of these sites is of critical importance as they play major roles in oxygen and substrate activation. In this study, we have used MCD spectroscopy applied to a wide range of mononuclear ferrous model complexes to obtain a rigorous correlation of excited-state spectral features and ground-state electronic structure with the geometric structure of a ferrous site. NIR MCD has been used to observe ligand field transitions, which correspond to the energies of the excited-state d-orbitals. VTVH MCD spectroscopy has been used to determine the sign of the zero-field splitting, to calculate ground-state spin-Hamiltonian parameters, and in the case of 6C and square pyramidal 5C sites, to obtain the ligand field splitting of the $t_{2g}$ orbitals of the ground state. For trigonal bipyramidal 5C and distorted tetrahedral 4C sites, the VTVH MCD data give insight into the $^5$E ground states. Combining these data produces an energy level diagram for the d-orbitals, and Figure 8 shows these diagrams for the ferrous complexes studied.

Ligand field theory has been used to provide a general model for correlating the excited-state splittings with the geometry of a given ferrous center.[3,6] Examination of the NIR MCD spectra collected for a wide range of ferrous models verifies the general ligand field trends and lends insight into why these trends occur. Experimentally, the 6C distorted octahedral ferrous models with N and O ligation (Figure 8, left) show two transitions centered at $10Dq$ ($O_h$) $\approx 10\,200$ cm$^{-1}$ and split by an average value of $\Delta^5E_g \approx 1800$ cm$^{-1}$. Square pyramidal 5C models (Figure 8, middle) have a larger average excited-state splitting, $\Delta^5E_g \approx 5700$ cm$^{-1}$ and show two transitions at $>10\,000$ and $>5000$ cm$^{-1}$. The 5C trigonal bipyramidal models (Figure 8, middle right) also have a large excited-state splitting, $>5000$ cm$^{-1}$, but show only one transition generally $<10\,000$ cm$^{-1}$, and the second transition is below the range of the NIR MCD instrument ($<4700$ cm$^{-1}$). 4C tetrahedral models show one transition at $<5000$ cm$^{-1}$, and distorted tetrahedral 4C models with predominantly N and O ligation (Figure 5, right) show two transitions at an average value of $10Dq$ ($T_d$) $\approx 7000$ cm$^{-1}$ with excited-state splittings of $<3000$ cm$^{-1}$. The origin of these trends can be understood in terms of the ligand field effects associated with the geometric structure of the ferrous site.

The small excited-state splitting for 6C sites is due to nearly equal ligand fields in the *x*, *y*, and *z* directions for a distorted octahedral complex. [Fe($H_2O$)$_6$]($SiF_6$) (Figure 8, **6a**) shows the smallest MCD excited-state splitting, $\Delta^5E_g = 1200$ cm$^{-1}$, which arises from the fact that the hexaaquo ferrous ion in the fluorosilicate lattice has only a slight $D_{3d}$ distortion from $O_h$.[14,64] In contrast, the hexaaquo ferrous ion site in Tutton's salt, [Fe($H_2O$)$_6$]($NH_4$)$_2$($SO_4$)$_2$ (**6b**), is more distorted[16] and consequently has a larger excited-state splitting, $\Delta^5E_g = 1600$ cm$^{-1}$. Removal of a ligand from an octahedral site to produce a 5C square pyramidal geometry causes the ligand field interactions along *z* to be significantly different than along *x*,*y*, and so, the square

(64) Hamilton, C. L.; Scott, R. A.; Johnson, M. K. *J. Biol. Chem.* **1989**, *264*, 11605$-$11613.

pyramidal complexes show a much larger average excited-state splitting than do the 6C models. The position of the highest-energy transition reflects metal−ligand $\sigma$-interactions in the equatorial plane of the square pyramidal site: stronger equatorial interactions will destabilize $d_{x^2-y^2}$ and increase the energy of the transition to this orbital, as illustrated by the high energy of this band for FeL(acac) (Figure 8, **5c**). In contrast, weaker equatorial interactions which lower $d_{x^2-y^2}$ are coupled with stronger axial metal−ligand interactions which increase the energy of $d_{z^2}$ so that the excited-state splitting is reduced, as seen for FeL(OAc) (Figure 8, **5a**).

Like the square pyramidal complexes, the trigonal bipyramidal 5C models also show a large excited-state splitting of $>5000$ cm$^{-1}$. These sites are distinguished by exhibiting only one transition in the NIR MCD spectrum at $\sim$10 000 cm$^{-1}$, whereas a second transition at $\sim$5000 cm$^{-1}$ is observed for square pyramidal sites. The high-energy transition, corresponding to the energy of the $d_{z^2}$ orbital, is below 10 000 cm$^{-1}$ for two of the trigonal bipyramidal models (Figure 8, **5h,i**) as predicted by ligand field theory, but lies at $>$10 000 cm$^{-1}$ for [Fe(trpn)(MeCN)]$^{2+}$ (**5j**), which has a stronger Fe−$L_{axial}$ interaction than the other models. Therefore, a single transition at $>$10 000 cm$^{-1}$ for trigonal bipyramidal species indicates a relatively strong metal−ligand interaction along *z*. The low energies of the ligand field transitions which are characteristic of the 4C models (Figure 8, right) correlate with the lower 10*Dq* values for tetrahedral vs octahedral sites ($10Dq$ ($T_d$) = ($-^4/_9$) $10Dq$ ($O_h$) in the crystal field limit). The splitting of the $t_{2g}$ excited-state orbitals varies over the series of distorted 4C models and the larger the orbital splitting, the more distorted the site, as seen for FeL(O-$C_6H_3$-2,6-$Cl_2$) (Figure 8, **4e**). Thus, with a few defined exceptions, the NIR MCD excited-state data provide a set of spectroscopic guidelines for determining the coordination number and geometry of a ferrous site and are complemented by the information content available from the ground-state data.

Once the geometry of the a ferrous site is known, the VTVH MCD ground-state analysis provides supplemental geometric and electronic structure information, which varies with coordination number. The 6C ferrous models generally show large values of $\delta$, $\delta > 4$ cm$^{-1}$, which are correlated with a small ligand field splitting of the $t_{2g}$ d-orbitals, $|\Delta| < 500$ cm$^{-1}$ (see Figure 8, left). Additionally, the 6C models show nearly rhombic splitting patterns, $|V/2\Delta| \approx 0.33$, which is understood in terms of small variations in the *x*, *y*, and *z* directions which are nearly equal in a distorted octahedral complex. ([Fe($H_2O$)$_6$]($SiF_6$) is the exception which has an axial ground-state splitting pattern, $|V/2\Delta| = 0.08$, due to the high site symmetry of the hexaaquo ferrous ion in the host lattice (vide supra).) Given that the $t_{2g}$ splittings are generally rhombic, the sign of the ZFS reflects the energy order of these three d-orbitals, −ZFS for the lowest-energy and middle orbitals closest in energy and +ZFS for the middle and highest-energy orbitals closest. Thus small changes in the geometry can shift the relative energy of the middle orbital and reverse the sign of the ZFS. It is important to recognize that for the near-rhombic 6C models, the nature of the ground-state d-orbital which contains the redox-active extra electron can be the same for both negative or positive ZFS and the sign in these cases merely reflects small structural differences at the site.

Two of the 6C models, [Fe(PMA)(MeOH)]$^+$ (Figure 8, **6d**) and [Fe(PY5)(MeOH)]$^{2+}$ (**6e**) show unusually small $\delta$ values and correspondingly large values of $|\Delta| \approx 1000$ cm$^{-1}$. This large splitting of the $t_{2g}$ orbitals is indicative of unique metal−ligand $\pi$-interactions at the site. In these models, the presence of $\sigma$-donor, $\pi$-acceptor ligands at short distances from the iron (pyrimidine in **6d** and pyridine in **6e**) gives rise to $\pi$-back-bonding which significantly affects the energy of the $t_{2g}$ d-orbital(s) involved. In fact, both [Fe(PMA)(MeOH)]$^+$ and [Fe(PY5)(MeOH)]$^{2+}$ show moderately intense low-energy metal-to-ligand charge-transfer (MLCT) transitions associated with $\pi$-back-bonding: the absorption spectrum of [Fe(PMA)(MeOH)]$^+$ shows multiple transitions at $\sim$13 000−20 000 cm$^{-1}$ ($\epsilon \approx 2000$ M$^{-1}$ cm$^{-1}$) which have been assigned as $Fe^{2+} \rightarrow$ pyrimidine MLCT transitions,[10] and [Fe(PY5)(MeOH)]$^{2+}$ shows one MLCT transition at $\sim$27 600 cm$^{-1}$ ($\epsilon \approx 1600$ M$^{-1}$ cm$^{-1}$).[19] The lower energy of the MLCT transitions for [Fe(PMA)(MeOH)]$^+$ indicates stronger $\pi$-back-bonding in this complex, which is reflected in the smaller $\delta$ value ($\delta = 2.4$ cm$^{-1}$) relative to [Fe(PY5)(MeOH)]$^{2+}$ ($\delta = 3.3$ cm$^{-1}$). Therefore, while 6C ferrous sites normally show a small orbital splitting of the ground state ($|\Delta| < \sim$500 cm$^{-1}$), larger splittings signal $\pi$-back-bonding at the ferrous site (along with the presence of low-energy charge-transfer bands), which can make a significant contribution to reactivity.

Compared to typical 6C complexes, square pyramidal 5C sites show smaller $\delta$ values, $\delta < 4$ cm$^{-1}$, and larger values of $\Delta$, $|\Delta| > \sim$800 cm$^{-1}$, resulting from the removal of a ligand along *z*. Within this range, the square pyramidal ferrous models fall into three categories: weak-axial, rhombic, and strong-axial. FeL(acac) (Figure 8, **5c**) and [Fe(TMC)Br]$^+$ (**5d**) are examples of the weak-axial square pyramidal species, in which the metal is only slightly shifted out of the equatorial plane. These models have small $\delta$ values ($\delta \lesssim 1$ cm$^{-1}$) and correspondingly large $-\Delta$ values ($|-\Delta| > 1500$ cm$^{-1}$) resulting from the weak interaction along *z*, which stabilizes $d_{xz}$ and $d_{yz}$, and from the metal being nearly coplanar with the equatorial ligands, which increases the energy of $d_{xy}$. As the metal is shifted out of the equatorial plane, the M−$L_{axial}$ interaction increases and the energy of $d_{xy}$ is lowered so that the $t_{2g}$ d-orbitals are closer in energy. This produces smaller values of $|\Delta|$ as seen for FeL(OAc), FeL(OBz), and [Fe(PMA)]$^+$ (Figure 8, **5a**,**b**,**e**), which have $|\Delta| \approx 800-900$ cm$^{-1}$. Rhombic distortions which split $d_{yz}$ from $d_{xz}$ are now on the order of the axial splitting so that that the three $t_{2g}$ orbitals are evenly spaced, producing rhombic splittings ($|V/2\Delta| \approx 0.33$) for these models. If the metal is shifted further out of the plane due to a strong axial interaction, then $d_{xy}$ becomes the ground state and a +ZFS system is produced. This is seen for [Fe(MeEDTrA)] (Table 5 and Figure 8, **5g**), which is less rhombic and has a positive value of $\Delta \approx +1000$ cm$^{-1}$. Thus, for 5C complexes, the magnitude of $|\Delta|$, which is inversely proportional to $\delta$, reflects the strength of the axial Fe−L bond: large and negative $\Delta$ values indicate a weak axial interaction, smaller values of $|\Delta|$ and rhombic splitting patterns indicate moderate-to-strong axial interactions, and positive $\Delta$ values indicate a strong axial bond.

The ground-state analysis for the trigonal bipyramidal 5C models shows that these are described by the −ZFS model with small $\delta$ values, $\delta < 2$ cm$^{-1}$. This is understood in terms of the high energy of the orbitals involved in out-of-state spin−orbit coupling with the ground state, E($d_{x^2-y^2}$, $d_{xy}$) $\approx$ 3000−4000 cm$^{-1}$, as compared to $|\Delta| \leq 2000$ cm$^{-1}$ for square pyramidal sites (see Figure 8, middle). Although 5C ferrous sites are often distorted between the limits of square pyramidal and trigonal bipyramidal geometry, it is important to recognize when the structure of a ferrous center is strongly distorted toward the trigonal bipyramidal limit as these sites lack an open coordination position for oxygen reaction. A strong indicator of the

geometry of a pentacoordinate ferrous site is the energy of the excited-state transitions, complemented by the ground-state information. Trigonal bipyramidal geometry is clearly identified when only a single transition is observed at $<10\,000$ cm$^{-1}$ and $\delta$ is $<2$ cm$^{-1}$. Likewise, a ferrous site cannot be trigonal bipyramidal if the VTVH MCD analysis yields a +ZFS ground state. Square pyramidal geometry is readily recognized if the excited-state transitions lie at $>5000$ and $>10\,000$ cm$^{-1}$ and the ground-state analysis yields $\delta = 3-4$ cm$^{-1}$ (rhombic-type square pyramid). Additionally, a square pyramidal-like geometry is assigned whenever two transitions are observed at $\sim$5000 and $\sim$10 000 cm$^{-1}$ since the associated lower-energy transition for trigonal bipyramidal sites lies below the range of the NIR MCD instrument. (The $\sim$10 000 cm$^{-1}$ band in square pyramidal centers can shift to lower energy for strong-axial sites and will shift to higher energy for weak-axial sites.) It is less clear as to which site geometry is appropriate when only one transition is observed at or above 10 000 cm$^{-1}$ and the ground state has a −ZFS pattern with $\delta < 2$ cm$^{-1}$. One possible assignment is a strong-axial trigonal bipyramidal geometry, in which the $d_{z^2}$ excited state is shifted to higher energy due to the strong axial interaction (for example, **5j** in Figure 8). Alternatively, a weak-axial square-pyramidal geometry with a large excited-state splitting and relatively low 10*Dq* value could cause the lower-energy band to shift below the instrument cutoff at $\sim$5000 cm$^{-1}$ so that a single band $\sim$10 000 cm$^{-1}$ with $\delta < 2$ cm$^{-1}$ is observed. With the exception of this case, the combination of excited-state transition energies and ground-state analysis provides sufficient information to recognize a 5C ferrous center which has approximate square pyramidal vs trigonal bipyramidal geometry and therefore an open coordination position for potential oxygen reactivity.

Although 4C ferrous active sites have been implicated in binuclear non-heme iron enzymes,[65] they have not yet been observed in mononuclear ferrous enzymes.[66] Nevertheless, it is important to be able to recognize the spectroscopic characteristics of a tetracoordinate ferrous ion. The ground-state analysis for the trigonally distorted 4C models shows that the sign of the ZFS correlates with the strength of the axial ligand: a strong axial bond produces −ZFS and a weak axial interaction produces +ZFS. The ground-state parameters determined from the VTVH MCD fit are similar to those obtained for other coordination numbers; therefore, the excited-state spectral features provide a more direct method for identifying 4C sites. As shown in Figure 8 (right), nearly tetrahedral 4C models have one characteristic ligand field transition at very low energy, $<5000$ cm$^{-1}$, and the distorted 4C models show two transitions in the 5000−7500 cm$^{-1}$ region, split by $<3000$ cm$^{-1}$. Therefore, 4C ferrous complexes are generally distinguishable from 6C sites, which show higher transition energies, and from 5C sites, which have larger excited-state splittings. As the distortions from tetrahedral geometry are more pronounced, the excited-state splitting may increase so that the spectrum of a 4C site may begin to look like that of a square pyramidal 5C site. FeL(O-$C_6H_3$-2,6-$Cl_2$) (Figure 8, **4e**) is an example of this, where the ferrous site is significantly distorted from the $C_{3v}$ parent symmetry and the position of the highest-energy band is near those observed for 5C complexes, although the smaller excited-state splitting in this example identifies the spectrum as resulting from a 4C species. As a tetrahedral ferrous site is further distorted toward square planar geometry, the energies and splitting of the two ligand field transitions increase,[3,6] approaching $\sim$8000 and $\sim$20 000 cm$^{-1}$ at the square planar limit, and a +ZFS ground state is expected.[67] Therefore, a case may arise in which the MCD spectral features in the 5000−13 000 cm$^{-1}$ region do not clearly distinguish between a 4C site which is strongly distorted toward the square planar limit and a near-rhombic or strong-axial (+ZFS) square pyramidal 5C site.

Thus the VTVH MCD results have been used to develop the information content available through the ground-state data for each coordination type. In 6C ferrous centers, the presence of unusually large $t_{2g}$ orbital splittings, $|\Delta| \approx 1000$ cm$^{-1}$, identifies strong $\pi$-back-bonding interactions, which may play a role in the oxygen reactivity of non-heme iron enzymes.[10,13] Because 6C sites generally show small $t_{2g}$ orbital splittings that are nearly rhombic, the sign of the ZFS does not provide specific electronic structure information. In contrast, the sign of the ZFS for square pyramidal 5C sites is an important indication of the strength of the axial bond. Weak-axial sites have −ZFS with $\delta < 2$ cm$^{-1}$ and a large $t_{2g}$ splitting ($|-\Delta| > 1500$ cm$^{-1}$), while increasing the axial strength produces a near-rhombic site with $\delta = 3-4$ cm$^{-1}$ and a reduced $t_{2g}$ splitting ($|\Delta| \approx 800$ cm$^{-1}$) until a strong-axial, +ZFS limit is reached. In trigonal bipyramidal 5C centers, the ground-state sublevel splitting is small, $\delta < 2$ cm$^{-1}$, due to the high energy of the excited states involved in out-of-state spin−orbit coupling with the ground state, and this small magnitude of $\delta$ may aid in distinguishing trigonal bipyramidal from square pyramidal geometry. For 4C ferrous centers, the ground-state analysis has been used to correlate the sign of the ZFS with the strength of the axial interaction in trigonally distorted tetrahedral sites and to obtain information about the ground-state d-orbital which contains the redox-active extra electron: a strong axial distortion produces a −ZFS system and a ground state which is mostly ($d_{x^2-y^2}$, $d_{xy}$), and a weak-axial trigonal distortion produces a +ZFS system and a ($d_{xz}$, $d_{yz}$)-like ground state.

Finally, the data from this study provide insight into the origin of the MCD intensity for ferrous sites. Expansion of the MCD *C*-term expression shows that two perpendicular nonzero electric dipole transition moments ($M_i$) are required: $\Delta\epsilon = g_z M_x M_y + g_y M_x M_z + g_x M_y M_z$.[48,68] For axially distorted 6C or 5C ferrous complexes, the E ground state has orbital degeneracy, as shown in Figure 9 (left) for the case of a $C_{4v}$ distorted square pyramidal site. Ligand field transitions from the $d_{xz,yz}$ (E) ground state to the $d_{z^2}$ ($A_1$) and $d_{x^2-y^2}$ ($B_1$) excited states are *xy*-polarized and should therefore exhibit nonzero *C*-term (and *A*-term) intensity. From the experimental MCD data, one finds that the orbital degeneracy of the ground state is removed due to rhombic distortions ($\delta \neq 0$) for all of the model complexes studied. Considering a rhombically distorted square pyramidal site with $C_{2v}$ symmetry[69] (Figure 9, right), transitions from the $d_{yz}$ ($B_2$) ground state to the $d_{z^2}$ and $d_{x^2-y^2}$ orbitals are electric dipole allowed only in the *y* direction. Without a second perpendicular transition moment, these transition will show no *C*-term intensity. However, transitions from the first excited state, $d_{xz}$ ($B_1$), to $d_{z^2}$ and $d_{x^2-y^2}$ are electric dipole allowed in the *x* direction

(65) Pulver, S. C.; Tong, W. H.; Bollinger, J. M.; Stubbe, J.; Solomon, E. I. *J. Am. Chem. Soc.* **1995**, *117*, 12664−12678.

(66) There is one crystal structure of the non-heme enzyme soybean lipoxygenase-1 which describes the ferrous active site as 4C (Boyington et al. *Science* **1993**, *260*, 1482). However, spectroscopic studies[11] and a recent low-temperature crystal structure at higher resolution (Minor et al. *Biochemistry* **1996**, *35*, 10687) indicate that an additional water ligand is also likely present in the 4C structure.

(67) Burns, R. G.; Clark, M. G.; Stone, A. J. *Inorg. Chem.* **1966**, *5*, 1268−1272.

(68) Thomson, A. J.; Cheesman, M. R.; George, S. J. *Methods Enzymol.* **1993**, *226*, 199−232.

(69) $C_{2v}$ is chosen as a low-symmetry point group in which all orbital degeneracy is lifted, but *x* and *y* transform as different irreducible representations.

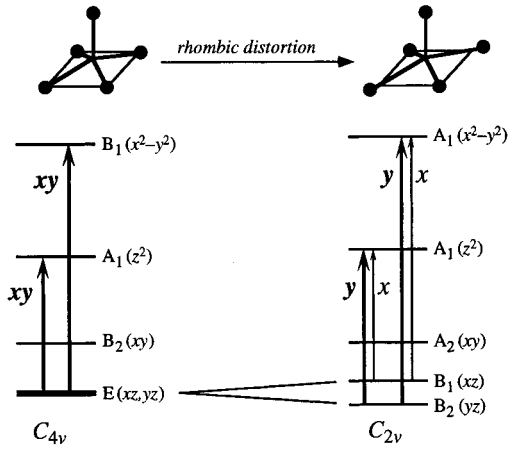


**Figure 9.** MCD selection rules for a square pyramidal site with $C_{4v}$ symmetry (left) and a distorted square pyramidal site with $C_{2v}$ symmetry (right) showing the direction of the electric dipole (*x*, *y*, *z*) allowed transitions from the $d_{xz}$, $d_{yz}$ ground-state components.

(Figure 9, right). Out-of-state spin−orbit coupling between the $d_{yz}$ and $d_{xz}$ orbitals will introduce some *x*-polarization into the *y*-polarized transitions from the ground state, thereby allowing for nonzero *C*-term intensity. (Transitions from the $d_{xy}$ orbital are electric dipole forbidden in this point group.) Thus spin−orbit coupling between the rhombically split components of the orbital ground state provides for the observed *C*-term intensity.[70,71] This is a different spin−orbit coupling mechanism than is often observed, for example, in copper complexes, where out-of-state spin−orbit coupling between excited states produces *C*-term intensities of opposite signs.[48,71,72]

Experimentally, one finds that most of the MCD transitions for the ferrous models studied are positively signed. For the low-symmetry point groups appropriate to these sites in which all orbital degeneracy is removed (e.g., $C_1$, $C_s$, $C_2$, $C_{2v}$), the $d_{x^2-y^2}$ and $d_{z^2}$ orbitals transform as the same irreducible representation (see Figure 9, right). When in-state spin−orbit coupling is included, the equivalent $M_S$ components of the $d_{x^2-y^2}$ and $d_{z^2}$ excited states will transform as the same spinor representation. Thus, a $\Delta M_S = 0$ transition from the lowest-energy spin−orbit-coupled component of the ground state to the $d_{x^2-y^2}$ excited state should have the same sign in the MCD as does the transition from the ground state to the equivalent $d_{z^2}$ component. There are, however, a few ferrous complexes (**5e**,**g**,**i**) which show negative MCD intensity for the highest-energy ligand field transition. It should first be noted that in these cases the structures of the ferrous complexes have not determined directly but are inferred from comparison to isomorphous analogues or from spectral data, and thus, these may, in fact, be greatly distorted from the related compounds. However, more limited structural distortions from the inferred ferrous geometry can also lead to the MCD sign reversal if the $d_{x^2-y^2}$ and $d_{z^2}$ orbitals transform as different irreducible representations, for example, through a $C_{2v}(\sigma_d)$ rather than a $C_{2v}(\sigma_v)$ distortion of the $C_{4v}$ parent geometry (i.e., one which approximately maintains a mirror plane between metal−ligand bonds rather than along bonds).[73] Further detailed insight into the MCD *C*-term signs and intensities for specific low-symmetry ferrous sites will require quantitative calculations using the spin−orbit-corrected many-electron wave functions and transition polarizations for these $d^6$ systems, such as has been performed for $d^9$ (one-hole) sites.[71,72,74,75] Thus, the *C*-term intensity mechanism for low-symmetry ferrous sites is found to arise from ground-state spin−orbit coupling between the rhombically split set of $d_{xz}$, $d_{yz}$ orbitals, and the fact that most of the transitions have the same positive sign may be understood in terms of the excited-state d-orbitals transforming as the same irreducible representation in the effective symmetry point groups appropriate to these models. This study has defined the information content of the VTVH MCD methodology for non-heme ferrous sites and should significantly aid in the analysis of parallel data on metalloproteins.

**Acknowledgment.** Thanks are given to Dr. Masami Ito, Tamako Ogihara, Dr. Kiyoshi Fujisawa, and Professor Yoshihiko Moro-oka for the synthesis of a number of the compounds used in this study and also to Professor T. D. P. Stack, Robert T. Jonas, Professor Karl S. Hagen, Dr. Tami E. Westre, and Dr. Susan E. Shadle for the donation of additional models. This research was supported by a grant from the National Institutes of Health (GM40392). The computing facilities of the Department of Chemistry at Stanford University are supported, in part, by a grant from the National Science Foundation (CHE-9408185).

**Supporting Information Available:** Mathematical derivation of the MCD intensity expression for non-Kramers systems including *z*-polarization, excited states, and temperature-independent *B*-terms; Gaussian resolutions for the overlapping bands in the MCD spectra of 6C and 4C models; and VTVH MCD data and fits for the complexes **6c**,**d**, **5a**,**c**,**d**,**j**, and **4d**−**g** (11 pages, print/PDF). See any current masthead page for ordering information and Web access instructions.

JA973735L

(70) Rivoal, J. C.; Briat, B. *Mol. Phys.* **1974**, *27*, 1081−1108.
(71) Gerstman, B. S.; Brill, A. S. *J. Chem. Phys.* **1985**, *82*, 1212−1230.
(72) Gewirth, A. A.; Solomon, E. I. *J. Am. Chem. Soc.* **1988**, *110*, 3811−3819.
(73) Wilson, E. B., Jr.; Decius, J. C.; Cross, P. C. *Molecular Vibrations. The Theory of Infrared and Raman Vibrational Spectra*; Dover Publications: New York, 1955.
(74) Landrum, G. A.; Ekberg, C. A.; Whittaker, J. W. *Biophys. J.* **1995**, *69*, 674−689.
(75) Farrar, J. A.; Neese, F.; Lappalainen, P.; Kroneck, P. M. H.; Saraste, M.; Zumft, W. G.; Thomson, A. J. *J. Am. Chem. Soc.* **1996**, *118*, 11501−11514.